ABSTRACT

Title of thesis: EXPERIMENTAL MEASUREMENTS OF VORTEX BREAKDOWN WITH NON-ISOTHERMAL INFLOW

Assaf Krupnik, Masters of Science, 2023

Thesis directed by: Professor Anya R. Jones
Department of Aerospace Engineering

Vortex breakdown occurs in many flow applications such as weather, aerodynamics, swirl combustors, and more, introducing unsteadiness that is often undesired. While vortex breakdown has been previously investigated extensively, researchers have struggled to efficiently characterize these flows due to the flow sensitivity to intrusive probes, and there is no real consensus regarding the process and reason of its formation. Recently, researchers have discovered the blue whirl, a silent and efficient flame which they believe is a mode of vortex breakdown, and suggested mechanisms of stabilization and prevention of it through temperature control. This thesis uses modern time-resolved measurement techniques to investigate breakdown at smaller temporal and spatial scales than previously researched, and shows the effect of heat addition at the inflow of a vortex generator on the onset and behaviour of breakdown modes.

Smoke flow visualization experiments were preformed to identify heating and swirl rate effects on vortex flow, and the resulting swirl angle of the flow was measured. Decreasing the incoming swirl was found to delay or fully suppress the formation of a breakdown bubble. Increasing the inlet temperature had a similar effect due to the buoyancy effects

on the flow increasing the axial velocity thus reducing the effective swirl. 3D Particle Tracking Velocimetry was used to obtain time-resolved flow fields of the vortex flow and breakdown with and without heating. Individual velocity profiles and velocity fields are presented, showing that flow behavior is dependent on much smaller scales than previously researched. Proper Orthogonal Decomposition is used to isolate energetically dominant modes and determine whether higher order modes are significant to the flow.

EXPERIMENTAL MEASUREMENTS OF VORTEX BREAKDOWN WITH NON-ISOTHERMAL INFLOW

by

Assaf Krupnik

Thesis submitted to the Faculty of the Graduate School of the
University of Maryland, College Park in partial fulfillment
of the requirements for the degree of
Masters of Science
2023

Advisory Committee:
Professor Anya R. Jones, Chair/Advisor
Professor Alison B. Flatau
Professor Johan Larsson

© Copyright by
Assaf Krupnik
2023

Acknowledgments

First and foremost, I would like to thank Dr. Anya Jones for the support, encouragement, and patience throughout my time working in her group. Since starting in the lab as an undergraduate, she gave me numerous incredible opportunities that helped me find my passion as an experimentalist. Dr. Jones' approach to mentorship and her belief in her students provide a work environment that is stress-free but fosters curiosity and hard work. I could not have asked for a better advisor.

I would also like to thank my lab mates, beginning with the senior members who were extremely patient and helpful as they taught me how to approach research. Jonathan Lefebvre, when I was a clueless undergrad, and Girguis Sedky, when I was a *still* clueless graduate student. To the current lab members, Antonios Gementzopoulos and Oliver Wild, you have helped me more than you know, both when I was picking your brains for ideas, and by being supportive when the work was getting frustrating. It is always more enjoyable to work with a friend around, especially in a dark, windowless room. I would also like to thank the undergraduate members of the lab that have helped in this research, Ao Huang, and particularly Andy Yeung, whose work developing the new fan was incredibly valuable to this project.

Special thanks are owed to my parents and siblings, for their ongoing support throughout my educational journey. Most importantly, I would like to thank my girlfriend, Molly, for always being my greatest supporter.

Finally, I would like to thank the National Science Foundation for supporting this research under NSF grant 2152596.

Table of Contents

Acknowledgements ii

1 Introduction 1
- 1.1 Motivation: The Blue Whirl . . . 1
- 1.2 Vortex Breakdown . . . 3
  - 1.2.1 Isothermal . . . 4
  - 1.2.2 Non-Isothermal . . . 6
- 1.3 Present Work . . . 7
- 1.4 Thesis Outline . . . 8

2 Experimental Setup 10
- 2.1 Vortex Breakdown Rig . . . 10
  - 2.1.1 Background and Development . . . 10
  - 2.1.2 Hardware Overview . . . 14
  - 2.1.3 Flow Heating . . . 17
- 2.2 Smoke Flow Visualization . . . 18
- 2.3 Particle Image Tracking . . . 19
- 2.4 Chapter Summary . . . 22

3 Smoke Flow Visualization 23
- 3.1 Overview . . . 23
- 3.2 Swirl Setting Variation . . . 24
- 3.3 Temperature Variation . . . 29
- 3.4 Swirl Angle Estimation . . . 31
- 3.5 Chapter Summary . . . 34

4 3D Particle Tracking Velocimetry 35
- 4.1 Overview . . . 35
- 4.2 Velocity Fields and The Breakdown Bubble . . . 37
- 4.3 Velocity Profile Analysis . . . 47
- 4.4 Proper Orthogonal Decomposition and Reconstruction . . . 51
- 4.5 Chapter Summary . . . 53

5 Conclusions 57
5.1 Summary 57
5.2 Open Problems and Suggestions for Future Work 59

A Heater Characterization 61

Bibliography 64

List of Tables

2.1 Nominal flow temperatures with $\alpha_{SV} = 0^o$ 18

3.1 Test matrix for smoke flow visualization experiments. Images from cases in red are shown in this thesis, B denotes observed breakdown. 24

4.1 Summary of PTV results presented in this paper. The rightmost column indicates whether breakdown was observed in the data 36

List of Figures

1.1 Evolution from a pool fire to a blue whirl. (A) Pool fire forms following ignition. (B) Canonical fire whirl develops subsequent to the pool fire. (C) Whirl evolves from a yellow fire whirl to a blue whirl. A cup-like blue whirling flame on water holds a yellow whirling flame. (D) Laminar blue whirl becomes clear. The vertical scale marked on the side of (A, B, and D) starts at the water surface. The height of the structure in (D) is about 15 cm. Adapted from Xiao et al. [35] 2
1.2 Bubble type breakdown evolving into spiral breakdown, axial flow from right to left. From Harvey 5

2.1 A variable-swirl vortex tube setup designed by Titchener and Taylor-Russel (from [33]). All dimensions are in inches. 11
2.2 A flow imaging setup for smoke flow visualization [16] 12
2.3 Horizontal velocity of the third and fourth POD modes of the rig flow . . . 14
2.4 Time history for POD modes shown in fig. 2.3 14
2.5 Schematic of the new rig design used in this study, including the initial fan design used in chapter 3 16
2.6 Cross section view of the intake assembly with the flow heater centerbody . 17
2.7 Schematic of setup used for PTV experiments 20
2.8 Schematic drawing of the field of view of an individual camera in the test section 21

3.1 Smoke flow visualization of case SV40T1.0 at two instances in time 26
3.2 Comparison of flow behaviour with a varying swirl vane setting θ_{SV} and no heating 28
3.3 Comparison of flow behaviour with a fixed swirl vane setting $\theta_{SV} = 40^\circ$ and increasing heater temperatures 30
3.4 Example of swirl angle estimation technique for case SV40T1.0 33
3.5 Example of swirl angle estimation technique for case SV40T0 33

4.1 Sample particle track results from STB for SV40T1.0 37
4.2 Velocity fields in the $r-z$ plane for the SV30T1.0 case over time. The colors represent the axial velocity component u_z and the vectors show the in-plane velocity. 39

4.3 Velocity fields in the $r-z$ plane for the SV40T1.0 case over time. The colors represent the axial velocity component u_z and the vectors show the in-plane velocity. 41
4.4 Velocity fields in the $r-z$ plane for the SV40T1.0 case with increased time resolution around time of peak breakdown bubble visibility. The colors represent the axial velocity component u_z and the vectors show the in-plane velocity. 42
4.5 3-D constant velocity contour for the SV40T1.0 case at time $T = t_0 + 0.95s$ indicating the near-stagnation regions in the flow 43
4.6 Velocity fields in the $r-z$ plane for the SV50T1.0 case over time 45
4.7 Velocity fields in the $r-z$ plane for the SV40T1.1 case over time 46
4.8 Mean velocity profiles along the radius at $z/R = 9$ for the vortex in SV30T1.0 48
4.9 Velocity fields in the $r-z$ plane for the SV40T1.1 case before, during and after the breakdown passes through the field of view 49
4.10 Select velocity profiles along the radius at $z/R = 9$ for the SV401.1 case corresponding to the flow fields shown in fig. 4.9. 50
4.11 Mean velocity profiles along the radius at $z/R = 9$ for the vortex in SV40T1.1 51
4.12 Velocity fields in the $r-z$ plane for the first four POD modes 52
4.13 Time coefficients for the first four POD modes, smoothed with a moving average low pass filter. 53
4.14 3-D constant velocity contour for the SV40T1.0 case at time $T = t_0 + 0.95s$ using the reconstructed flow fields from the first four POD modes 54
4.15 Image of a breakdown bubble at $Re_t = 6500$ captured at $10Hz$, from [27] . 55

A.1 Time-Averaged velocity field for case SV00T13, The colors represent the axial velocity component u_z and the vectors show the in-plane velocity . . . 62
A.2 Temperature map at the $r-z$ plane measured with $T_h = 323K$ 63

Chapter 1: Introduction

In the concluding remarks of a 1988 review of vortex breakdown research, Escudier wrote "It is both remarkable and unsatisfactory that a phenomenon which in many respects is as 'simple' as, and even similar to, the shock wave, hydraulic jump and boundary-layer separation, should still be the subject of disagreement as to its fundamental nature."[10] Thirty-five years later, not much has changed. Vortex breakdown has been researched extensively, but fundamental understanding of its onset and behavior is still lacking compared to other flow phenomenons. While this thesis does not presume to unequivocally resolve the mystery of vortex breakdown, the never before use of novel tools to investigate it advances the field in that direction.

1.1 Motivation: The Blue Whirl

Vortex breakdown is an extensively researched phenomenon with documented occurrence in a variety of fields and flow regimes where unsteady flow is present, such as weather, aerodynamics (e.g. delta wings, rotating wings, Formula 1 cars), swirl combustors, and more. The inherently unsteady nature of reacting, non-isothermal flows makes breakdown a prime interest in the fields of fire research, where researchers have recently discovered the blue whirl, a silent yet distinctly efficient form of flame with a variety of potential uses, which is a unique form of the more common fire whirl [35]. Fire whirls, in general, are intense turbulent diffusion flames characterized by a standing vortex composed

of wind and fire that occur naturally in fires when the right combination of fuel, topography, and airflow creates an eddy.

In laboratory settings, fire whirls can be created through various experimental setups involving fuel ignition [9][23][22][31] or studied through numerical simulations [1][30] [2][5]. However, the blue whirl represents a more complex phenomenon that has been observed spontaneously when a hydrocarbon burns on a smooth flat surface. The transition from a fire whirl to a blue whirl in a laboratory experiment is shown in figure 1.1. During this transition, a blue flame forms at the bottom of the standing vortex, initially remaining attached to the surface [5]. Subsequently, the yellow spiral flame collapses. This transition typically completes within approximately seven seconds, transforming a violent fire whirl into a seemingly calm and stable blue flame [19].

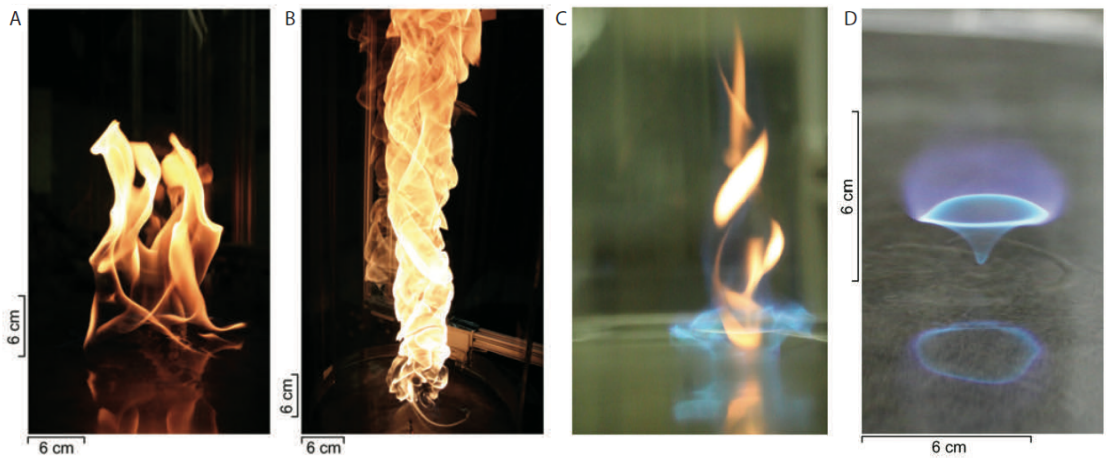


Figure 1.1: Evolution from a pool fire to a blue whirl. (A) Pool fire forms following ignition. (B) Canonical fire whirl develops subsequent to the pool fire. (C) Whirl evolves from a yellow fire whirl to a blue whirl. A cup-like blue whirling flame on water holds a yellow whirling flame. (D) Laminar blue whirl becomes clear. The vertical scale marked on the side of (A, B, and D) starts at the water surface. The height of the structure in (D) is about 15 cm. Adapted from Xiao et al. [35]

Since its discovery in 2016, the stability and lack of turbulence in the blue whirl has attracted significant research interest. Further experiments have provided insights into the formation conditions and characteristics of the blue whirl. Temperature maps [15], chemi-

luminescence measurements [14], new scaling laws [18], and a summary of swirl vane angles that produce stable blue whirl conditions [7] have been obtained. However, the measurement of the flame and flow structure of the blue whirl remains extremely challenging.

Recent numerical simulations investigating the evolution of the blue whirl and vortex breakdown in fire whirls suggest that the blue whirl consists of three different flames: a diffusion flame, a premixed rich flame, and a lean flame, converging into a fourth structure known as a triple flame—a whirling blue ring [6]. While computationally expensive and complex, these simulations provide valuable information about blue whirl and fire whirl behavior, reactive vortex breakdown, fluid dynamics, and reactive flow instabilities.

The discovery and study of the blue whirl have led to the hypothesis that it represents a form of vortex breakdown within a fire whirl. However, the onset and maintenance mechanisms of this mode remain unclear. One hypothesis, supported by simulations [36], suggests that local variations in heating due to the motion of burning material within the fire whirl may trigger the transition to a blue whirl. In this study, heat was added to or extracted from a fire whirl vortex breakdown bubble, resulting in a stabilization of the bubble with heat addition and return to a coherent vortex with heat extraction. Replicating the simulation in an experiment will be extremely difficult due to the unpredictability of reacting flows required to produce the required heating values at the breakdown bubble. However, better understanding of breakdown mechanisms in non-reacting cases, may provide significant insight that could be extended to studies of the blue whirl.

1.2 Vortex Breakdown

Since it was first named and discussed in the 1930s, vortex breakdown research has been spread across several fields and time periods. Particularly, advances in experimental

and numerical techniques have led to surges in research output at certain times. Lately, improvements in imaging and processing technology have facilitated advancements in many fluid dynamics research areas. Vortex breakdown, which has been mostly studied computationally in recent years, can benefit immensely from the precise velocimetry measurements currently available.

1.2.1 Isothermal

In the late 1960's, Harvey [16] and others studied vortex breakdown experimentally by generating a vortex in a stationary tube, and varying the ratio of tangential to axial velocity, commonly referred to as the swirl ratio, within the range expected to result in vortex breakdown, based on prior numerical investigations. Figure 1.2 shows smoke flow visualization from Harvey [16] in which the core is seen expanding to a bubble structure, which then reforms into flow similar to the core before dissipating into the vortex and forming a spiral. His experiments, and others [11], [27], relied primarily on flow visualization methods for determination of flow structures, which tend to lack the time and spatial resolution required to fully characterize unsteady flows, and use of physical probes in the flow, which were found early on to disturb or affect the highly sensitive breakdown behavior [16] [4]. In an attempt to mitigate those issues, Faler and Leibovich [12] preformed similar experiments in water while also measuring time averaged velocity profiles of the transition using non intrusive Laser Doppler Anemometry (LDA). While the use of LDA sidesteps the issues of affecting the flow, it was limited to time averaged velocities and did not provide any high time resolution data.

Despite the limitations of the methods used, these early works provide a basic idea of the conditions required for vortex breakdown. several researchers have found that the location of breakdown along the vortex axis can be controlled. Lowson [24] changed the

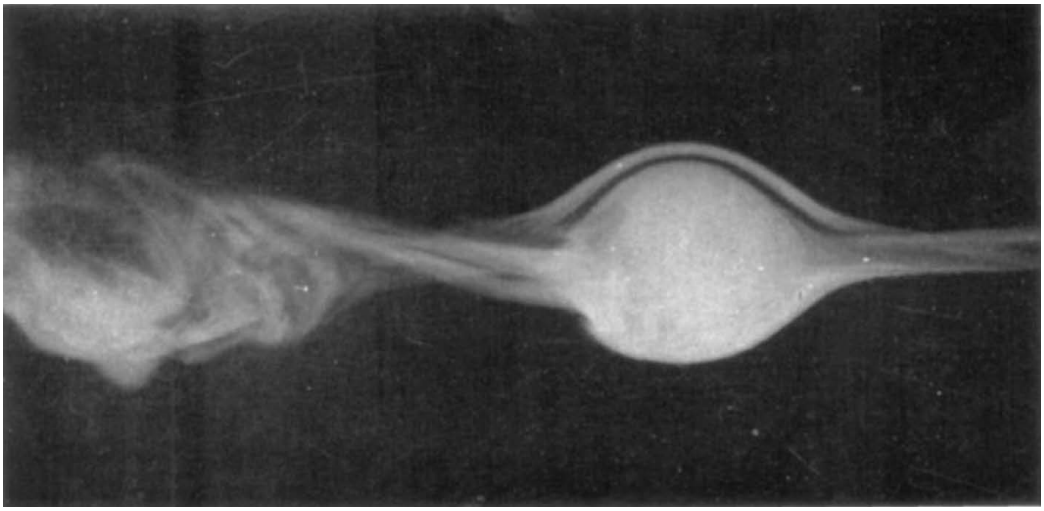


Figure 1.2: Bubble type breakdown evolving into spiral breakdown, axial flow from right to left. From Harvey

chord length of a delta wing experiencing breakdown, Cassidy and Falvey [4] partially blocked the end of a test section tube, and Sarpkaya [27] constricted the end of a similar test section. In all three cases, it was observed that by effectively creating a 'more adverse' pressure gradient, breakdown can be induced and moved upstream. Hall [13] has further found that the pressure gradient does not need to be induced externally, but could also be caused internally by the vortex dynamics. Escudier [11] found that for an inviscid flow that could be approximated as a Rankine vortex:

$$\left(\frac{dp}{dx}\right)_0 = \left(\frac{dp}{dx}\right)_\infty + \frac{2\rho}{\delta^3}\left(\frac{\Gamma_\infty}{2\pi}\right)^2 \frac{d\delta}{dx} \tag{1.1}$$

Where the left hand side is the pressure gradient on the axis, the first term on the right hand side is the imposed pressure gradient due to external swirl, and Γ is the imposed circulation. The second term in the right hand side is the internal contribution to the gradient, which is positive if the core grows, and becomes more significant if the core is smaller, circulation is increased, or the core expands more rapidly [25]. Similar theoretical work by Krause [20] has shown using a basic momentum analysis that if the core grows in the

streamwise direction, breakdown must always eventually occur, agreeing with the general theory that an adverse pressure gradient will cause breakdown.

This theory regarding basic conditions for breakdown led to experiments in various converging and diverging tubes, which identified three types of breakdown: double-helix, spiral and bubble-type (axisymmetric) [27]. (Some later publications refer to double-helix and spiral as variations of the same type.) Types were shown to evolve into other types in some conditions, and the occurrences were shown to be governed by the Reynolds number and swirl number of the flow. In some conditions, periodic transition or hysteresis loops ay occur, resulting in an even less steady breakdown [32][27].

Limited work using time resolved techniques to investigate breakdown have been published. Bruecker used early Particle Tracking Velocimetry method combined with volume scanning to measure quasi-3D velocity fields of a breakdown bubble [3] and spiral [**?**]. He was the first to identify internal structures in the breakdown bubble, characterized by a vortex ring inducing axial flow reversal, with the vortex portion expanding around the bubble. This proposed structure explains flow structures identified in the breakdown wake [27]. Further, the vortex ring is tilted relative to the axis and gyrates periodically, and the stagnation point caused by the flow reversal similarly oscillates about the axis. These finding were limited, however, by the limitations of analog imaging at the time, resulting in a very low ($< 10Hz$) time resolution, which restricts the ability to investigate some unsteady behaviors.

1.2.2 Non-Isothermal

The study of vortex breakdown in compressible and non-isothermal flows, particularly in swirl combustors and fire protection, has led to several studies into effects of various heating methods on the breadkown. Herrada and Shtern [17] numerically investigated ef-

fects of a global temperature gradient acting axially on a vortex. Their study found that an axially increasing temperature suppresses breakdown, while the opposite gradient induces and stabilizes it. In studying the blue whirl, Zhang et. al. [36] approached the non-isothermal problem differently, by directly heating or cooling a breakdown bubble. In their study, they computationally generated a simplified case of swirling flows with heat addition and extraction using the unsteady, compressible Navier-Stokes equations with a source term in the energy equation. The bubble breakdown mode was found to grow in size when heated, while remaining stationary. The spiral mode downstream was gradually suppressed, and eventually stabilized into a coherent axial vortex core. These simulations suggest that control of vortex breakdown through heat addition may be possible if heat can be artificially controlled in the bubble. Notably, the required inputs are reversed to those found by Herrada and Stern, meaning any possible control must be spatially precise to avoid opposite results to the desired ones.

Difficulties in controlling the existence and location of pressure gradients in reacting flows, and physical limitations of heat addition without any reactions have mostly limited non-isothermal investigations to computational and numerical methods. Experimentally, Rukes et al. [26] used a heating element in a swirling jet, so that heat could be added to the axis of the breakdown bubble. Heating has been found to have an effect on suppressing or allowing spiral breakdown in some cases, due to the density profile of the flow. However, the studies required a intrusive heating element, which may have affected the flow, and the flow velocity was much higher than that exhibited in a fire whirl or blue whirl.

1.3 Present Work

The present work seeks to use modern time-resolved velocimetry tools to enhance the body of knowledge on breakdown onset and mechanisms in general, and specifically when

heat is added. While the heat addition process is strictly non-reacting, the author hopes this and subsequent works can influence blue whirl onset research. The experiments presented in this thesis were designed using previous work and adapted to allow better temporal and spatial resolution. The objectives of the current work are:

1. Design and build an experimental rig capable of reliably generating vortex breakdown, with a non-intrusive inflow heater and Particle Tracking Velocimetry capabilities.

2. Explore the effects of heating on the breakdown process and compare with similar simulations

3. Demonstrate that time-resolved 3D measurements of vortex breakdown are obtainable and explore the new data they provide.

1.4 Thesis Outline

Chapter 2 details the design process of the experimental rig used in this thesis, including the changes made to existing designs and some preliminary experiments that influenced the final design. It further shows the experimental methods used for the smoke flow vizualisation and PTV experiments, detailed in chapters 3 and 4, respectively.

Chapter 3 shows smoke flow visualization images for varying swirl and temperature, shedding light on breakdown conditions and general structure, and concludes with an analysis of trends in the flow swirl angle relative to changes in the independent variables.

3D Particle Tracking Velocimetry results are detailed in chapter 4. Velocity fields of various flow conditions, including breakdown, are presented, and the data is used to analyze the velocity profiles and variability in the different flow phases. Proper orthogonal

decomposition is used to identify dominant modes in the flow. Finally, chapter **??** summarizes the data and corresponding open problems, and suggests future work that can follow.

Chapter 2: Experimental Setup

This chapter describes the development of the vortex breakdown rig used for the experiments in this thesis, including an inflow heater and optical access for PIV (Particle Image Velocimetry) or PTV (Particle Tracking Velocimetry) measurements. A characterization of the flow heater is given, as well as a detailed description of the flow visualization and PTV techniques that were used.

2.1 Vortex Breakdown Rig

2.1.1 Background and Development

A variety of experimental rigs were used in prior research to investigate vortex breakdown. The design of the rig used in this study utilizes principles from a number of them, but is fundamentally based on a design first used in 1957 by Titchener and Taylor-Russel [33]. The rig design, shown in figure 2.1, is comprised of an annular contracting intake with variable swirl vanes, and a centerbody spike to turn the flow towards the test section. A diffuser and fan were installed downstream to control the axial flow velocity. Pressure taps and probe access holes were incorporated in the test section for various flow measurements.

Harvey adapted this rig design to capture smoke flow visualization images, using the setup shown in figure 2.2. His design added a small inlet for smoke in the intake centerbody, and used an angled mirror between the light source and camera to avoid any glare that may be caused by the tube curvature.

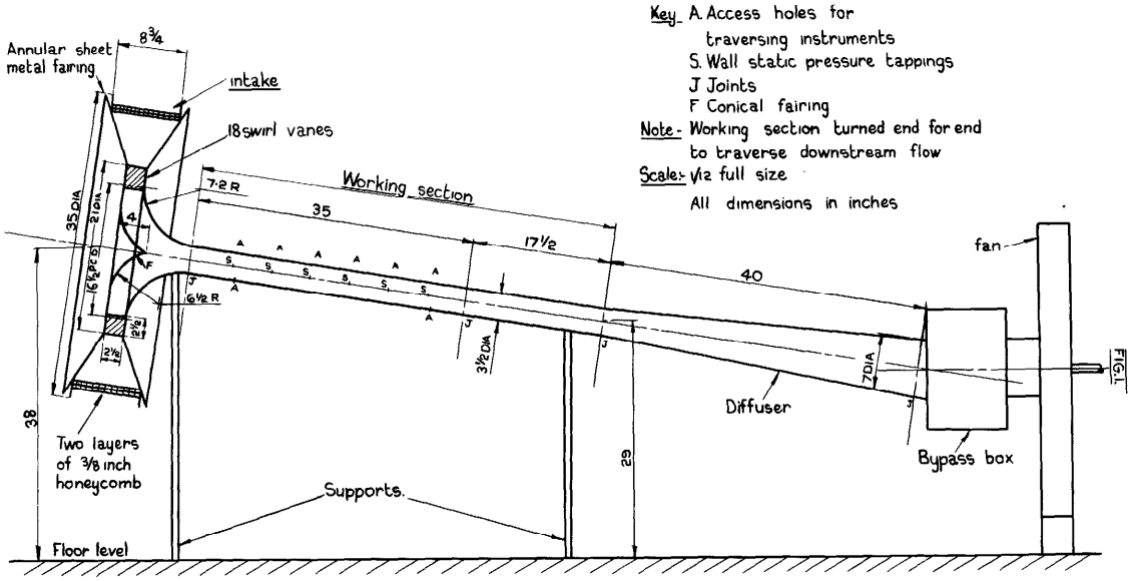


Figure 2.1: A variable-swirl vortex tube setup designed by Titchener and Taylor-Russel (from [33]). All dimensions are in inches.

Harvey's rig design was chosen as a basis for the newly designed rig for a number of reasons. The intake geometry allows for incorporation of a heating element in the centerbody without the introduction of any intrusive devices that may have unwanted effects on the flow, the separated controls for flow angularity and axial velocity allow a more detailed investigation of flow parameters affecting breakdown occurrence, and the limited volume of the test section (versus an open jet setup, for example) is more suitable for particle image measurements since the seeding density is easier to control. To ensure that the conditions that allowed reliable generation of breakdown in Harvey's rig, the overall dimensions were conserved.

The changes made for the current design were driven by the main goals of the current study. The intake plenum was redesigned with a circular hole at its center to accommodate a replaceable centerbody that can house a flow heater or seeding inlet as needed. The gauze used by Harvey to condition the inflow had to be removed to prevent any filtering of seeding particles, which influenced an enlarged intake design with more swirl vanes

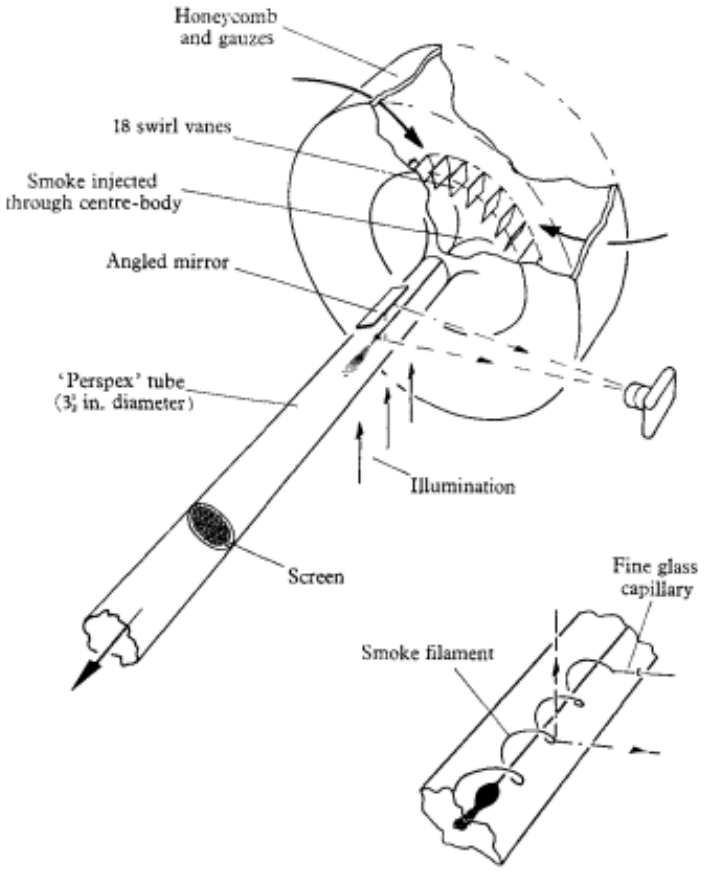


Figure 2.2: A flow imaging setup for smoke flow visualization [16]

and a higher flow contraction ratio to decrease incoming flow turbulence. A borosilicate glass tube was selected due to its heat resistance and ability to withstand laser illumination. However, initial experiments with illumination through the tube have proven it difficult to prevent reflection and refraction through the tube that interfered with imaging due to tube imperfections and curvature. Therefore, the drive section of the rig was completely redesigned, with an annular, belt driven fan with an optical and instrument access hole in its center. The pressure gradient induced by the hole also acts as a replacement for the diffuser in the original design, resulting in a much simpler to manufacture test section.

The rig design iterations used for the experiments presented in the following chapters are presented in section 2.1.2. A preliminary 2D PIV study was preformed with an early rig

iteration to test the viability of the setup. The majority of the results of this study are beyond the scope of this thesis, and can be found in a prior publication [21]. However, a particular finding had significant influence on the centerbody design. The vortex core diameter correlates to the centerbody tip width [27], which influenced a rounded-bluff tip design for the original centerbody. The experiments showed a highly unsteady vortex behavior with only momentarily visible breakdown modes characterized by vortex core oscillations about the center axis. Figure 2.3 shows the in-plane horizontal velocities from Proper Orthogonal decomposition (POD) of the third (left) and fourth (right) modes found in the time resolved measurements of vortex flow in the test rig. The modes show a strong horizontal velocity of opposing signs along the tube's central axis. A time history of the modes' appearance in the measurement is shown in figure 2.4, which shows that the modes are generally occurring in an equal but opposite pattern. This pattern indicates possible oscillations of the vortex perpendicular to the image plane, such that at different times, the PIV flow field captures the edges of the core. The periodic, oscillatory motion appears consistent with bluff body vortex shedding, and was hypothesized to be caused by the geometry of the centerbody. Indeed, a sharp 'trailing edge' was incorporated in the rig, and resulted in much more stable observed flow. Additional adjustments were made prior to preforming the PTV experiments, particularly a redesign of the fan assembly to reduce complexity and vibrations. Since both fan assemblies were used in experiments presented in this thesis, they are both described in detail in section 2.1.2.

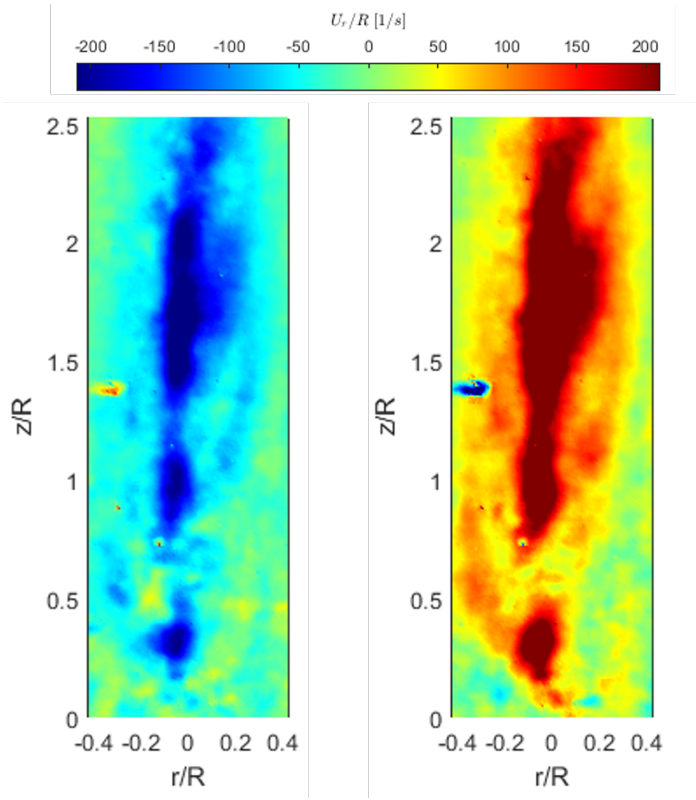


Figure 2.3: Horizontal velocity of the third and fourth POD modes of the rig flow

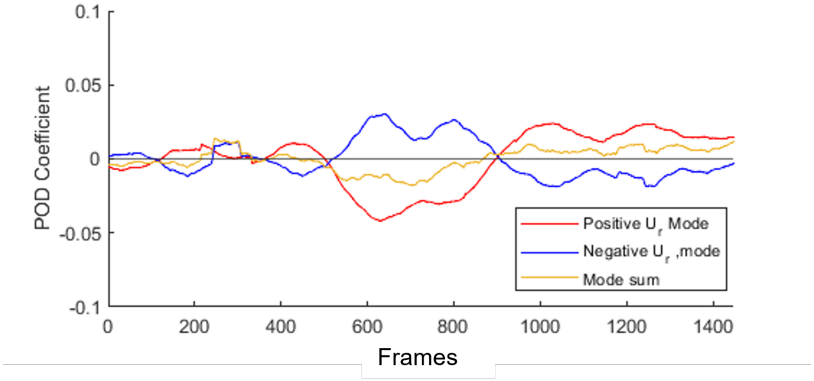


Figure 2.4: Time history for POD modes shown in fig. 2.3

2.1.2 Hardware Overview

A schematic drawing of the complete rig design is shown in figure 2.5. Rather than the slanted mounting previously used, a vertical orientation was preferred to aid with alignment

of the laser beam parallel to the test section. The rig is comprised of three main portions. The driving section at the top of the figure includes a 1.5 horsepower motor, which uses a belt (not shown) to drive a hollow shaft connected to the annular fan. The shaft has a constant inner diameter of $d_{OA} = 50mm$ for optical and instrument access. The hollow shaft and the gap between the fan shroud and the test section tube allow for an adverse pressure gradient to develop.

The test section is made of a SIMAX Borosilicate 3.3 tube with an inner diameter $D_t = 95\,mm$ ($R_t = 47.5\,mm$), $2.5\,mm$ thickness, and a length of $750\,mm$. No pressure tap or sensor holes were added to allow for clear imaging from any angle.

A cross section of the intake assembly at the bottom of the rig is shown in detail in figure 2.6. Air enters through an annular opening and is contracted to the test section at a ratio of 9:1. 30 NACA0012 swirl vanes with a chord length of $c_{sv} = 50.8\,mm$ allow for adjustment of the flow rotationality, which along with the fan speed control allows setting of the flow swirl angle. The bottom of the intake plenum is made of 3D printed PLA, and the top, clear, portion is made of cast acrylic.

The centerbody includes an embedded $1/4\,in$ diameter, $4\,in$ long Watlow FIREROD insertion heater with a built in type K thermocouple for heating control, which is held in with high conductivity thermal paste. The heater is controlled using an EXTECH 48VFL11 PID controller with a temperature measurement accuracy $< 1\%$ over the range of temperatures used. The centerbody is made of solid tellurium copper, which was chosen for its combination of high thermal conductivity of $350\,W/M-k$ and ease of machining relative to pure copper. A layer of high temperature ceramic fiber insulation separates the copper from the PLA plenum to prevent warping under high heat. The plenum surface was sealed, smoothed and sanded to ensure an undisturbed boundary layer along the surface until the trailing edge at the tip of the centerbody. The test section inlet, which acts as the origin for any results shown in this thesis, begins $3\,mm$ downstream of the heater tip.

A second variation of the drive section was used for the PTV experiments and can be seen in figure 2.7. The freestanding fan assembly was replaced with a small 3D printed shroud with an identical diameter to the original fan of $d_{OA} = 50mm$. The shroud is outfitted with four Noctua NF-A6x25 FLX $60mm$ diameter fans each with a max flow rate of $29.2m^2/h$. The fans, which are designed for low vibrations, are mounted to the assembly with anti-vibration pins, resulting in significantly less vibration than the original fan, and consequently more stable flow through the rig. With either fan assembly, the rig can generate zero swirl freestream velocities up to $1.4m/s$. While the original fan is capable of higher motor speeds, the resulting increase in vibrations limited their use.

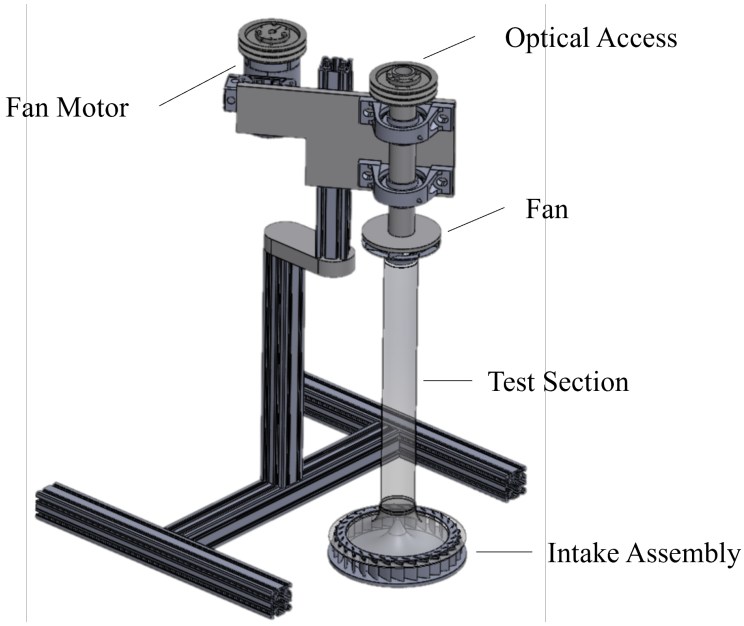


Figure 2.5: Schematic of the new rig design used in this study, including the initial fan design used in chapter 3

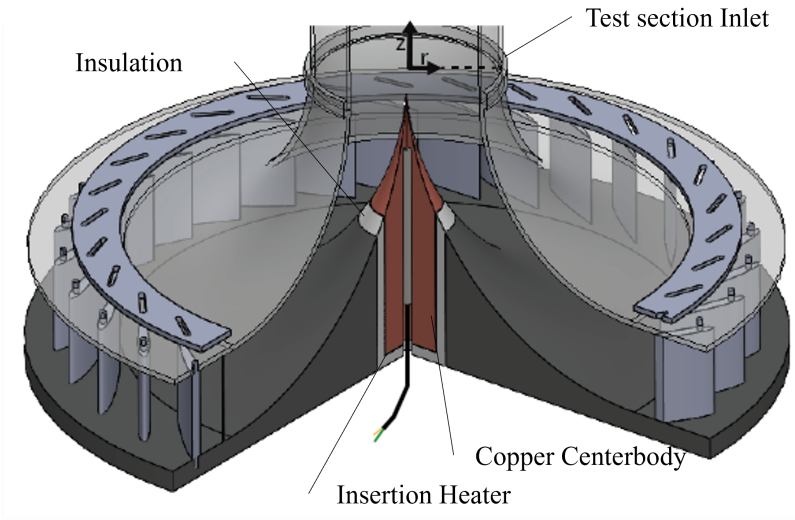


Figure 2.6: Cross section view of the intake assembly with the flow heater centerbody

2.1.3 Flow Heating

The cartridge heater is rated for a maximum temperature of $1033\,K$, but the intake assembly can only accommodate constant temperatures $\leq 450\,K$, up to $550\,K$ for short periods before deformation or burning occurs. Constant temperature heating was applied during experiments to prevent overheating.

Preliminary temperature measurements were done to asses the heating effect of the assembly on the flow using a Blue Robotics MS5837 digital pressure and temperature sensor, traversed radially from central axis to the test section wall and axially between $z = 0$ and $80\,mm$. The measurements were done with a swirl vane angle $\alpha_{SV} = 0^o$ and a freestream temperature $T_\infty = 295\,K$. For each spatial sweep at a certain temperature setting, the minimum, maximum and average temperatures were calculated. A summary of the findings is shown in table 2.1. Each row corresponds to a specific heater setting. The data shown in the table in order is: the heater temperature in Kelvin, the minimum, maximum, and average temperature normalized by the freestream temperature, the flow

Reynolds number based on the local density and tube diameter, and the flow axial velocity. Due to the small spatial gradients, mean values are used for Reynolds number calculation, and the heating is assumed to be uniform. For a more detailed explanation of the temperature and velocity measurements that led to this assumption as well as the Reynolds number estimation with regards to the variable density, see appendix A.

$T_h(K)$	$T_{t,min}/T_\infty$	$T_{t,max}/T_\infty$	$T_{t,av}/T_\infty$	Re_D	$U_z(m/s)$
295	0.99	1.0	1.01	7026	1.1
323	1.03	1.04	1.04	7541	1.25
373	1.05	1.07	1.05	7635	1.3

Table 2.1: Nominal flow temperatures with $\alpha_{SV} = 0^o$

2.2 Smoke Flow Visualization

Smoke flow visualization images were collected using the rig setup shown in figure 2.5. A 300 lumens LED spotlight was mounted above the drive section to project light through the optical access hole and illuminate the center portion of the test section. Smoke was injected near the trailing edge such that the filament separated near the tip using a Chauvet H1200 fog machine, which vaporizes 'fog juice' - a 3:1 mixture of water and plant glycol. Images were collected using a NIKON D800 DSLR camera with a 50mm focal length lens at a distance $D_c = 4R_t$ from the tube central axis, which was mounted on a vertical traverse to allow imaging at different points along the test section. A low exposure time was used to capture instantaneous flow and reduce background noise, yet some images have been additionally post-processed to adjust colors or remove background objects. No other edits were made.

2.3 Particle Image Tracking

A 4 camera 3D PTV system was used to collect reliable time-resolved data over the volume without relying on a minimal steadiness of the core and the axissymetric assumption. The Shake-The-Box (STB) algorithm was used to reconstruct particle tracks. Shake-The-Box extends principles of Tomographic PIV to allow fast and accurate tracking of particles in a measurement domain by predicting the location of particles found in previous frames, and utilizing an image matching scheme likened to 'shaking' the particles within the 'box' to identify individual particles across all cameras [29]. STB has been shown to produce comparable accuracy result to Tomographic PIV, at processing times 3 to 4 times faster.

The setup used for the PTV experiments is shown in figure 2.7. The vortex rig was placed on a hydraulic lifting table, to allow traversing the test section along its axis without moving the cameras or light source optics. A PS23 Rocket vaporizing fog machine and a mean particle size of $0.2-0.3\mu m$ was used to seed the air around the rig and allow the smoke to be entrained to the test section through the intake for uniform particle distribution. The seeding was illuminated using a dual-head Photonics DMX-30-527 Nd:YLF laser with up to $100mJ$. The laser beam was directed through a 7-mirror articulating arm to a volumetric optic device consisting of two cylindrical lenses with an effective divergence half-angle of 3°, and clipped using a circular aperture to remove the non-uniform portions of the volume. The low divergence angle resulted in an effective uniform radius volume through the camera FOV. The particle images were acquired using four high speed cameras, two Phantom V641s and two Phantom VEO640s, with a 2650 X 1600 resolution and an acquisition rate of $800Hz$ and Nikkor lenses with a focal length of $50mm$ set to $f/16$ for increased image depth of field. The cameras were positioned in a fan configuration with a constant radius $R_c = 10R_t$ from the test section central axis, and a spread angle $\beta = 20^\circ$ between cameras for a total fan angle of 60°.

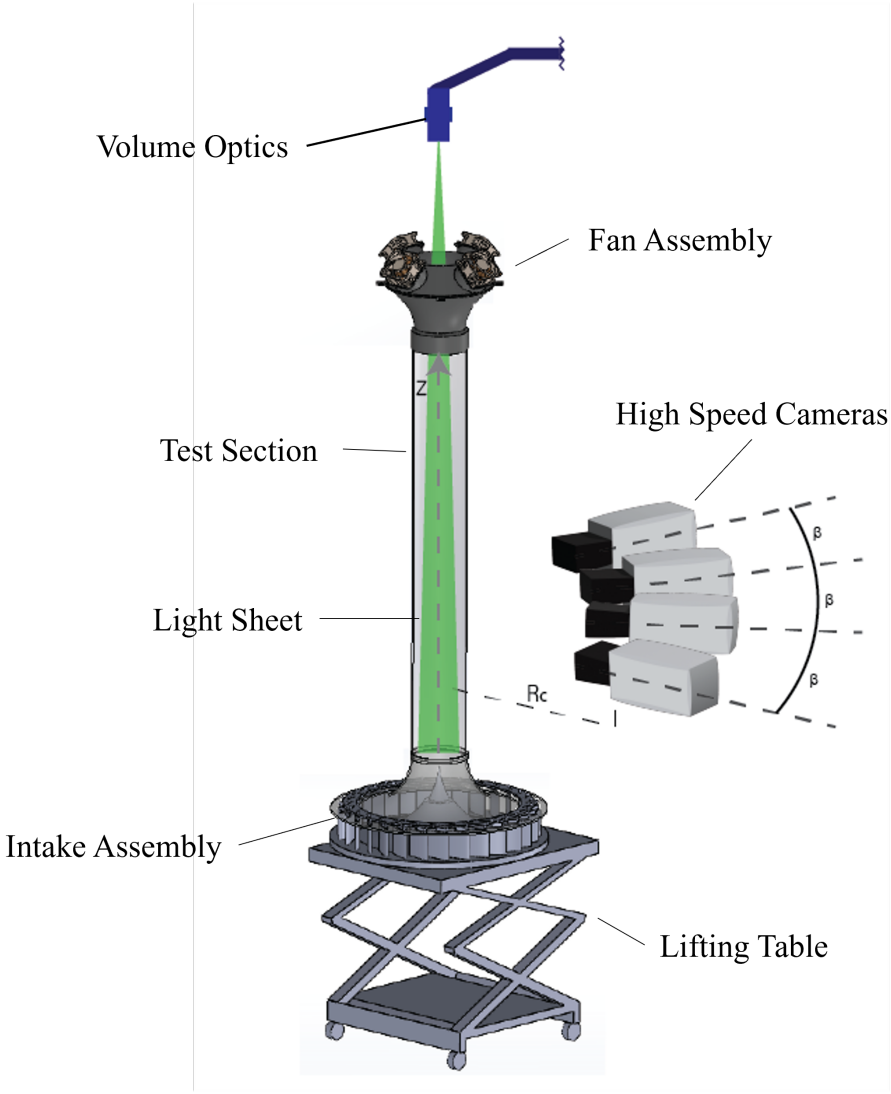


Figure 2.7: Schematic of setup used for PTV experiments

Figure 2.8 Shows a drawing of the test section as viewed by a single camera. The dashed red line indicates the camera field of view, while the blue dashed line shows the effective field of view, where particles were illuminated, which was used to extract the particle tracks. Since the flow is reliably axissymetric outside the core and possible breakdown, the light sheet and volume of interest were slightly offset, to capture the vortex core as well as a larger portion of the vortex.

The STB algorithm relies on calculation of a local optical transfer function (OTF) for

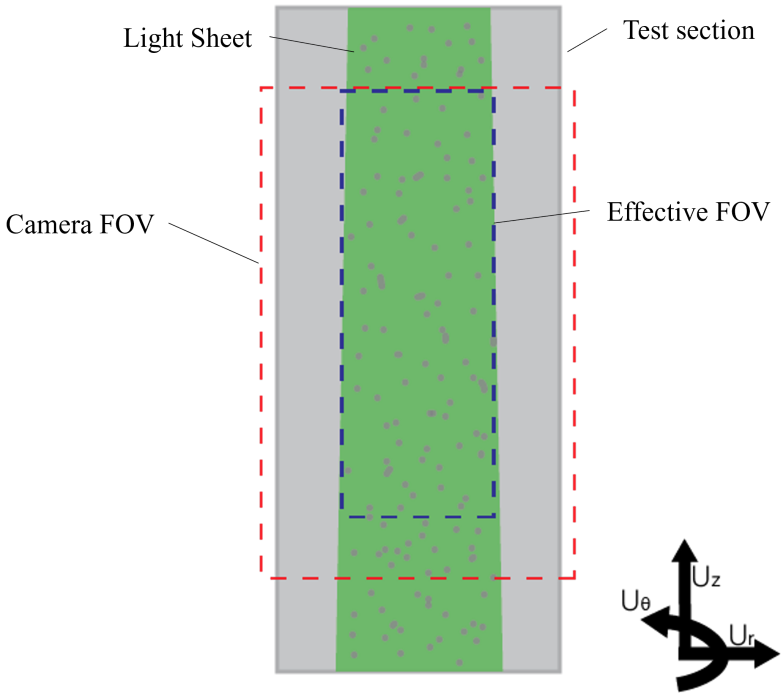


Figure 2.8: Schematic drawing of the field of view of an individual camera in the test section

sub-volumes in the field of view to assist with detection of ghost particles and image matching [28]. The OTF can be calculated using a volumetric self calibration process, which utilizes the STB iterative particle reconstruction algorithm to identify any disparities between the particle positions in the cameras estimated using the planar calibration method commonly used in 2D PIV. Due to the high degree of freedom in this system and potential for significant changes to the image due to optical distortion from the curved tube at even the smallest movements, the OTF was independently calculated for each data set prior to processing, with disparities ≤ 0.05 voxel .

The STB implementation in LaVision's DaVis 10 software was used to find the particle tracks. A physics informed finite scale reconstruction algorithm was used to convert the Lagrangian tracks to Eulerian grid velocity fields for analysis.

2.4 Chapter Summary

This chapter described the experimental setup used for the experiments presented in this thesis. The development process for the vortex rig was shown, including the adjustments made to the original design used by Harvey [16] to allow for flow heating and PTV measurements, as well as later adjustments that were made based on preliminary experiments.

The rig design was shown in detail, focusing on the drive-section and the intake. Two drive section designs were used in the experiments. A belt driven annular fan with a hollow shaft for lighting was used for the smoke flow visualization experiments, but that design was prone to vibrations that introduced unsteadiness to the flow. A compact fan assembly using a 3D printed duct and four computer fans was used for the PTV experiments. The intake design includes swirl vanes with a variable angle, as well as a plenum centerbody with a flow heater capable of maintaining a constant temperature. Temperature measurements are shown, which indicate lower flow temperatures than those of the heater, but heated flow nonetheless.

An overview of the specific methodology for each experiment presented in this thesis was given. Smoke flow visualization images were taken by injecting a smoke filament near the centerbody and into the vortex core. The smoke was illuminated using an LED light and images were taken with a DSLR camera. 3D 4-camera time-resolved PTV experiments were preformed at $800Hz$ and processed into velocity fields using the Shake-The-Box algorithm.

The rig and experiment designs described in this chapter are a critical portion of the work presented in this thesis, as a significant portion of this project relied on the ability to perform these experiments with any certainty or repeatability. As such, the development of the rig required extensive work to achieve a working model suitable for the research problems at hand.

Chapter 3: Smoke Flow Visualization

This chapter presents the smoke flow visualization results. Images of flow structure for a variety of heating temperatures and swirl vane angles are shown, and variation in flow swirl angle is estimated. These primarily qualitative results are used to predict flow behavior and identify cases of interest for further investigations, as well as to compare the flow behavior to that described in the literature.

3.1 Overview

The high number of independent variables in this study results in too large a number of cases to investigate effectively with PTV due to its high processing time. Flow visualization is a powerful, often overlooked tool which can produce data that is relatively easy to collect and interpret quickly. The smoke flow visualization results presented in this chapter cover the entire range of heater temperatures and swirl vane angles. Table 3.1 summarizes the cases that were investigated. For each swirl vane angle θ_{SV}, the flow heater was set to constant temperatures at $50K$ intervals. The top row represents experiments with no heating, such that the flow temperature $T = T_\infty = 295K$. Flow images for cases marked in red are shown in this chapter. Data from cases shown in black are used in this chapter, but the images are not included. Results from the lone case marked in blue were not used, as it was intended to test the limits of the method, and was found to produce unusable images, whether due to increased smoke dissipation at higher temperatures, additional smoke from

burning sealant around the heater, or a combination of both. For each case, an 'X' marks no observed breakdown within the field of view, and a 'B' marks an observed breakdown bubble or spiral. For brevity, cases are referred to in this paper by notation of the form 'SVXXTY.Y', where 'XX is the swirl vane setting in degrees and 'Y.Y' is the rounded first two digits of the heater temperature ratio T_h/T_∞. (i.e SV40T1.0 corresponds to a swirl vane angle $\theta_{SV} = 40^\circ$ and Temperature ratio $T_h/T_\infty = 1.0$.)

Table 3.1: Test matrix for smoke flow visualization experiments. Images from cases in red are shown in this thesis, B denotes observed breakdown.

		$\theta_{SV}(^\circ)$			
		20	30	40	50
T_h/T_∞	1.00	X	B	B	B
	1.09	X	X	B	B
	1.26	X	X	B	B
	1.43	X	X	X	B
	1.60	X	X	X	X
	1.77			X	

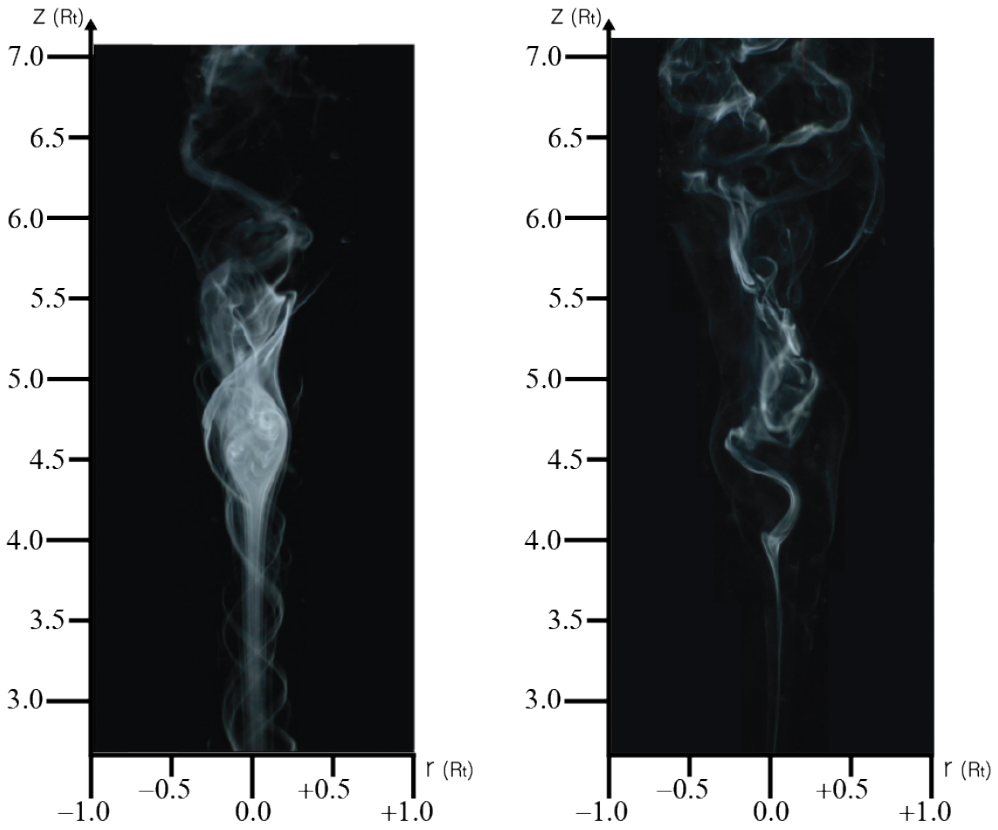
3.2 Swirl Setting Variation

Initial experiments were performed with no heating to identify the flow behavior in relation to the swirl vane angle θ_{SV} setting. A setting of $\theta_{SV} = 40^\circ$ was chosen as the baseline case, since it was expected to reliably cause breakdown while still allowing a margin to increase the angle before reaching the critical swirl angle estimated by various researchers to be $\theta_{S,max} \approx 51^\circ$ [27]. Figure 3.1 shows two images captured at different times for the SV40T1.0 case. Figure 3.1a on the left resembles the so called axissymetric bubble mode and figure 3.1b on the right most closely resembles the spiral mode. The flow alternates somewhat periodically between the two modes, with the point of breakdown beginning around $z = 4R_t$ (where R_t is the tube radius) and traversing axially downstream before

dissipating and reforming. While such behavior could be explained by instabilities in the inflow caused by ambient disturbances or intake surface imperfections, some previous findings may shed light on the observed phenomenon. Expanding on the work of Talbot [32], Sarpkaya [27] defined regions of breakdown behavior based on flow Reynolds Number, Re_t, and circulation number, $\Omega = \gamma/U_\infty - D_t$. Above $Re_t \approx 2000$, only bubble and spiral mode breakdown can occur, with the choice of which depending on the circulation number. Furthermore, a region of hysteresis exists between the two, in which the flow would periodically transition from one to the other. With $Re_t \approx 7500$, the flow conditions in these experiments fall well within the hysteresis region, which would provide an explanation for the unsteady behaviour. Ultimately, this behavior provides an opportunity to investigate several phases of breakdown flow, though the increased unsteadiness makes data collection more challenging.

A closer look at the bubble mode image in figure 3.1a provides a glimpse into the internal structure of the breakdown bubble not often seen previously, which is possible due to the axial lighting, rather than perpendicular lighting that may reflect off the bubble's external shell. Upstream of the bubble, where $z \leq 4.25R_t$, the core can be seen, with several streamlines of the vortex around it. The majority of the smoke is in the core, showing that the bubble is predominantly fed by it. At $4.25R_t \leq z \leq 5.0R_t$, the bubble can be seen, beginning with slight swelling of the core, followed by two counter-rotating vortices reminiscent of a bluff-body wake. While it is presumed by many to be axissymetric, the vortex pair, which in three dimensions should form a vortex ring, appears to be tilted relative to the rotational plane $r - \theta$. The region downstream of the bubble $z \geq 5.0R_t$ is slightly more dissipated, but it appears that the turbulent wake of the bubble gets mixed in with the remaining rotating flow outside the bubble to form a weak, wide spiral with some rotation.

Figure 3.2 shows smoke flow visualization images for the range of swirl vane angles tested. Note that SV50T1.0, shown in fig. 3.2d, was captured at a lower z position to ac-

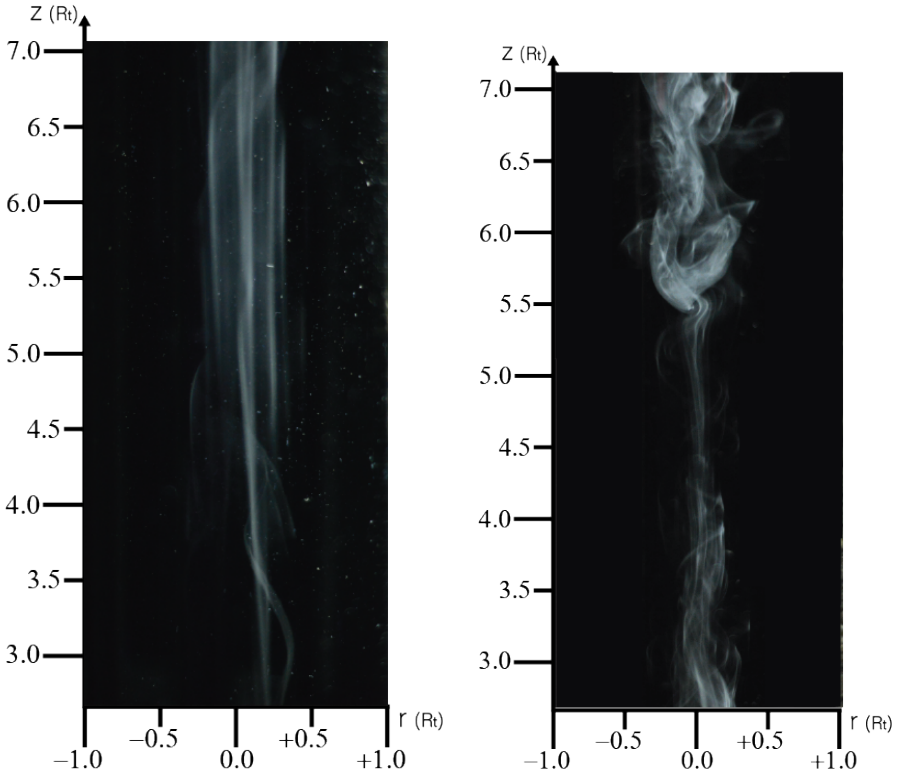


(a) Bubble Mode (b) Spiral Mode

Figure 3.1: Smoke flow visualization of case SV40T1.0 at two instances in time

count for the earlier observed breakdown. The results follow the expected behavior, showing more pronounced breakdown occurring further upstream as the swirl increases. Figure 3.2a shows SV20T1.0, in which the core appears to remain coherent, with minor diameter perturbations. This structure remained stable in time and no breakdown was observed at any axial position. When the swirl setting is slightly increased to SV30T1.0 shown in fig. 3.2b, a similar stable core is observed, although a breakdown structure is evident at $z \geq 5.5R_t$. It is difficult to determine from this image the type of breakdown exhibited, but there appears to be an element of axissymetry which would imply a bubble mode. Regardless, the collapse of the vortex into a supercritical mode is clear. Figure 3.2c again shows SV40T1.0 which appears earlier in this section. The breakdown bubble clearly occurs up-

stream of the observed breakdown in SV30T1.0 and is much more pronounced. Finally, figure 3.2d shows SV50T1.0, in which a breakdown structure similar to that of SV40T1.0 appears. While the smoke density is slightly reduced due to increased instabilities in the intake at higher swirls resulting in less detail in the bubble, the counter-rotating vortices that form the vortex ring can be seen with an opposite tilt to the one in SV40T1.0. Additionally, the breakdown occurs at an earlier axial position, around $z \geq 3.2$.



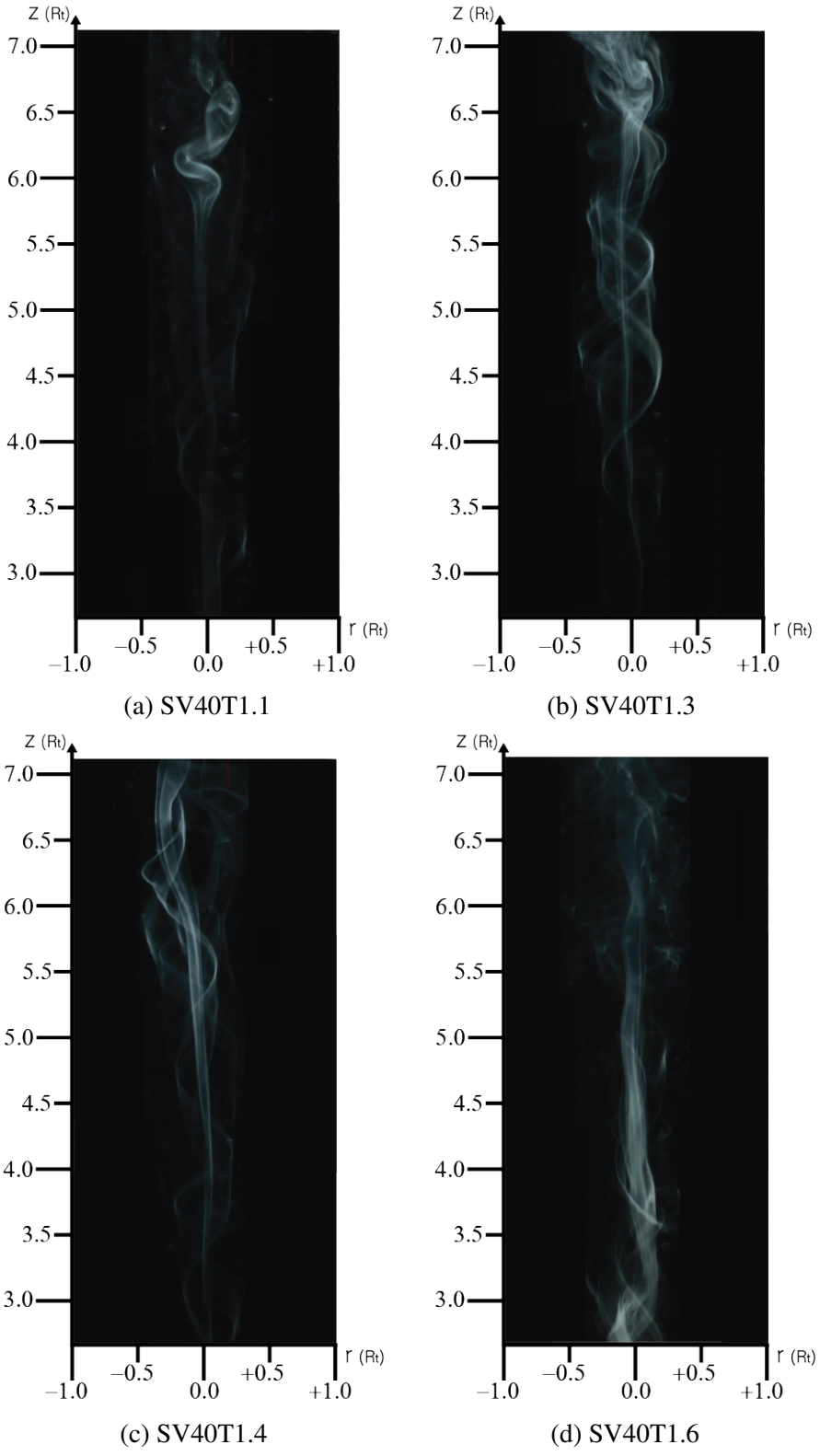
(a) SV20T0.0 (b) SV30T0.0

(c) SV40T0.0 (d) SV50T0.0

Figure 3.2: Comparison of flow behaviour with a varying swirl vane setting θ_{SV} and no heating

3.3 Temperature Variation

Images were taken at increasing heater temperature settings for each swirl setting. Figure 3.3 shows the flow for a swirl vane angle $\theta_{SV} = 40^\circ$ at increasing temperatures. This particular swirl vane setting is shown due to the range of possible behaviors exhibited by the flow. At the lowest heating value in SV40T1.1, shown in fig. 3.3a, breakdown is clearly exhibited further downstream than with no heating, beginning at $z = 5.75R_t$. Rather than a bubble mode or periodic behavior, the flow in this case only produces a spiral mode at all times. As the heating is increased in SV40T1.3 shown in fig. 3.3b, the breakdown is observed even further downstream at $z = 6.5R_t$. At even higher heating values of SV40T1.4 and SV40T1.6 shown in figs. 3.3c 3.3d respectively, breakdown is no longer observed. However in the former there is slight core swelling similar to that occurring upstream of observed breakdown indicating possible breakdown further downstream, and in the latter the core appears to remain coherent throughout the test section. The results suggest that the heating has a stabilizing effect on the vortex, delaying breakdown or preventing it altogether. Similar trends were observed when heating was applied at other swirl vane settings. The heating effect also resembles the behavior of the flow when the swirl vane angle is reduced.



(a) SV40T1.1 (b) SV40T1.3

(c) SV40T1.4 (d) SV40T1.6

Figure 3.3: Comparison of flow behaviour with a fixed swirl vane setting $\theta_{SV} = 40^\circ$ and increasing heater temperatures

3.4 Swirl Angle Estimation

The similarities between the effects of heating and of changing the swirl vane angle can be investigated by comparing their respective influences on a physical quantity, such as the flow swirl angle θ_s. Figure 3.4 shows a sample swirl angle θ_S measurement for SV40T1.0 at three axial positions. Some of the smoke separates from the centerbody into the core, while some enters the vortex and forms a streamline that can be measured to determine its angle with the z axis. The accuracy of results from this method is not guaranteed, due to limited precision while measuring visually on an image, and the requirement to follow visible streamlines that are not necessarily following the exact same radius spiral for each case. Nonetheless, these measurements provide a good, partially quantitative understanding of the effects of the independent variables on breakdown onset.

Upstream of a bubble, the swirl angle increases as z increases, due to the adverse pressure gradient in the tube reducing the axial velocity while the rotational velocity remains mostly unchanged. In the example in figure 3.4, which shows a bubble type breakdown for SV40T1.0, the three measured swirl angles are $\theta_{s_1} = 42.9^\circ$, $\theta_{s_2} = 46.3^\circ$, and $\theta_{s_3} = 54.7^\circ$. Numerous researchers have shown that a 'critical' swirl angle, above which breakdown must occur, is in the range of $\theta_{s,max} \approx 51^\circ$ [27][16][10]. Thus, the measured value of θ_{s_3} is consistent with the exhibited breakdown immediately downstream of the measurement point.

The same technique can be applied to estimate the swirl angle for the range of cases measured. Figure 3.5 summarizes the swirl angles for each case measured as closely as possible to $z = 4.25R_t$. Each symbol represents a swirl setting, and the horizontal axis shows the heater temperature ratio T_h/T_∞. For SV50, the lowest two heating settings are not shown since breakdown occurred upstream of the measurement point, making it impractical to measure the swirl angle at that position. For the smallest swirl vane setting SV20, which

exhibited no breakdown, the swirl angle appears to remain mostly constant with a very slight decrease as the heating increases. However, at increased swirl vane angles, heating seems to decrease the swirl angle significantly, at a roughly similar slope. This decrease in θ_s explains the lack of observed breakdown, as the flow does not reach the critical swirl angle required for it to occur.

A brief analysis of the effect of the heating on the flow dynamics is required to explain the reduction in θ_s. At a steady low velocity in the test section, well below the compressible flow regime, the Boussinesq approximation can be used to simplify the Navier-Stokes equation for a buoyancy driven flow [34]:

$$\frac{Du}{Dt} = \frac{1}{\rho_0}\nabla p + \nu\nabla^2 u - g\rho \tag{3.1}$$

Where $\rho \approx \alpha\Delta T$, with α the thermal expansion coefficient of air and ΔT the change in temperature and ρ_0 is approximated as constant. For an unheated flow, the fan creates a favorable pressure gradient which drives the flow through the test section until it reaches steady state, where the acceleration is 0. This approximated form indicates that for an increase in temperature from the steady state, the only change is caused by the temperature change introducing a favorable pressure gradient, which increases the axial velocity in the test section, in turn reducing the swirl angle $\theta_s = \tan^{-1}\left(\frac{u_\theta}{u_z}\right)$, until a new steady state is reached.

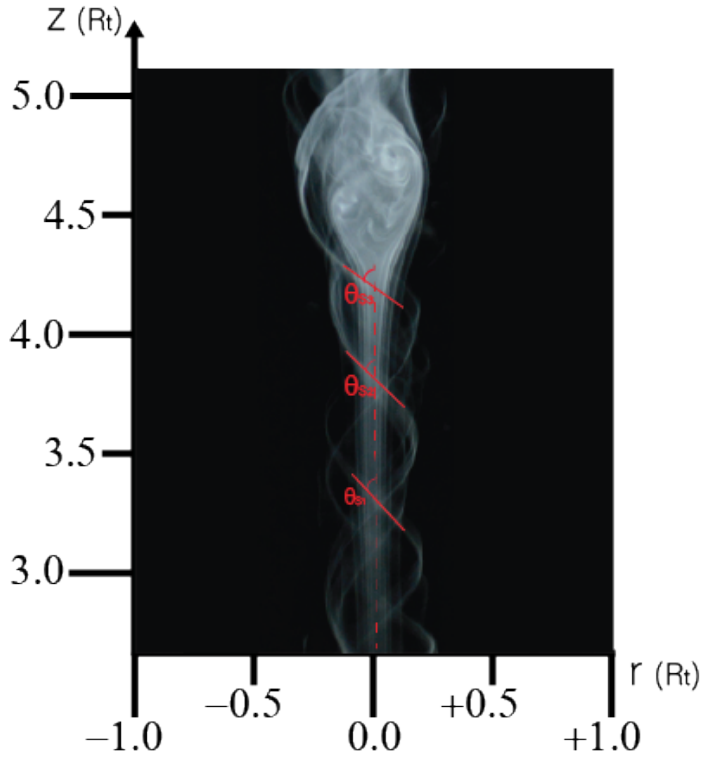


Figure 3.4: Example of swirl angle estimation technique for case SV40T1.0

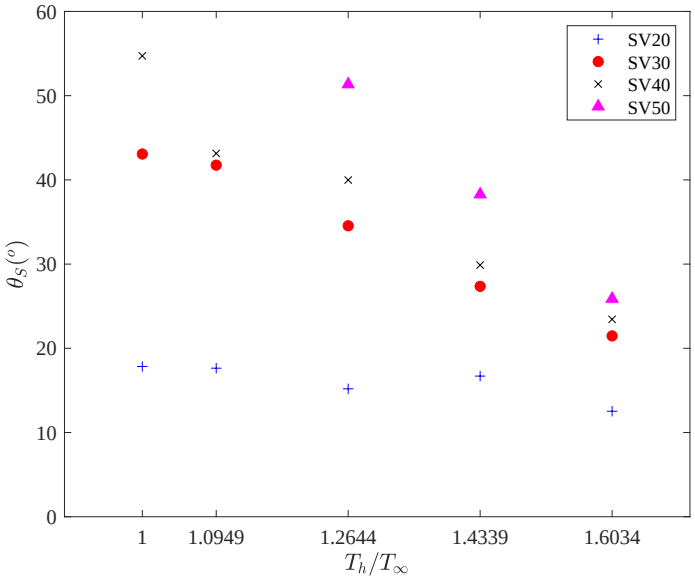


Figure 3.5: Example of swirl angle estimation technique for case SV40T0

3.5 Chapter Summary

This chapter showed smoke flow visualization images of the vortex flow with a varying swirl vane angle and heater temperature. The images were used to determine the conditions necessary for breakdown and the breakdown mode, as well as the effect of the independent parameters on the flow behavior. For the baseline case SV40T1.0, the flow was shown to be periodically changing with both a bubble and spiral mode occurring interchangeably. This may be due to the flow being within an identified hysteresis region identified by Sarpkaya [27], which may cause oscillations between the spiral and bubble mode. Changing the swirl vane angle setting θ_{SV} was shown to inversely affect the z position of the breakdown occurrence, with the smallest setting, SV20, not resulting in breakdown at all. Visualizations of increasing heating values for SV40 were presented, showing a delay in the breakdown and stabilization of the vortex, similar to the decreasing swirl vane angle. A summary of the swirl angles, as estimated visually from the vortex streamlines, indicated a similar trend for all swirl vane settings. Finally, the Boussinesq approximation was applied to the Navier-Stokes equation to explain the effects of heating on the flow buoyancy and consequently its dynamics, which showed that uniform heating applied upstream of a flow opposing gravity increases the vertical adverse pressure gradient strength, which results in increased axial velocity and decreased swirl angle. This effect is the most likely cause of the delayed breakdown with increased heating.

Chapter 4: 3D Particle Tracking Velocimetry

This section presents time-resolved three-dimensional Particle Tracking Velocimetry (PTV) measurement results for select cases. Select velocity fields are shown, including ones containing breakdown. Changes in axial and rotational velocities throughout the breakdown process are investigated and presented. Proper Orthogonal decomposition (POD) is used to identify modes in the flow during breakdown, and the flow is reconstructed using only the dominant modes.

4.1 Overview

Time-resolved velocimetry measurements are a powerful quantitative tool that has not been extensively applied to investigate vortex breakdown and may provide valuable insight into its behavior. For the highly three-dimensional and unsteady flow addressed in this thesis, three dimensional measurements were critical to investigate breakdown and the effect of heat on it. Specifically, four camera 3D PTV was used with Shake-The-Box (STB), as described in chapter 2. A sample particle tracking result is shown for case SV40T1.0 in figure 4.1, where each track indicates the position of a particle over five time steps. A recirculation bubble can be seen around $z/R = 2.0$, denoted by the blue region showing negative axial velocity. These particle tracks can then be used to obtain Eulerian velocity fields for further analysis. In this chapter, four cases of swirl and heating settings were selected and measured, as summarized in table 4.1. Two-dimensional axial velocity (u_z) fields of flow

along the vortex core in the $r-z$ plane are presented for all cases. An analysis of velocity profile changes over time for the steady vortex observed in SV30T1.0 is presented and compared with SV40T1.1, since the latter is a unique case where flow upstream, downstream, and in the bubble is captured in one data set. POD is used with flow fields from SV40T1.0 to compare the flow reconstructed using the dominant modes to the actual flow measured. Table 4.1 indicates no observed breakdown in SVT30T1.0, despite a bubble having been observed in the smoke flow visualizations. This is likely due to the limited field of view for the PTV measurements resulting in a smaller span of the test section being included in the measurements. Note that the measured flow fields are offset, with the z axis slightly to the left of the center, since the axissymetric assumption implies that the vortex is the same on either side of the core, so the field of view was selected to maximize the area of unique flow that is captured.

Table 4.1: Summary of PTV results presented in this paper. The rightmost column indicates whether breakdown was observed in the data

Case	Flow Fields	Velocity Profiles	POD	Breakdown?
SV30T1.0	X	X		
SV40T1.0	X		X	X
SV40T1.1	X	X		X
SV50T1.0	X			X

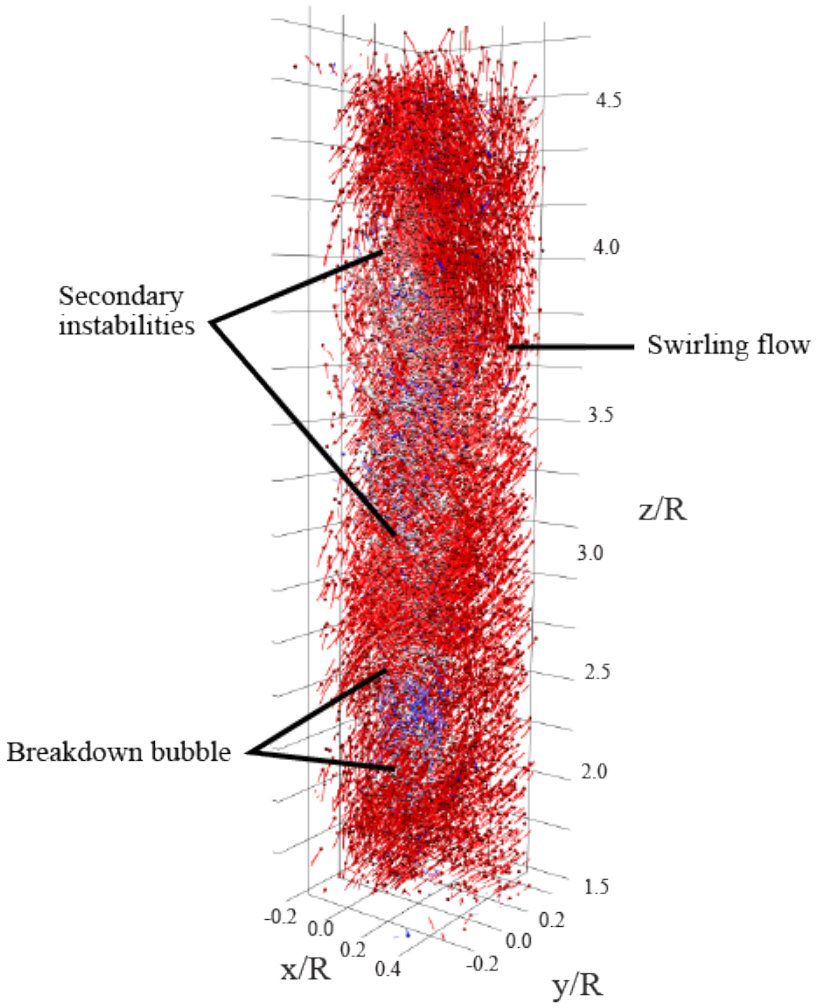


Figure 4.1: Sample particle track results from STB for SV40T1.0

4.2 Velocity Fields and The Breakdown Bubble

Three dimensional velocity fields are fundamentally difficult to present in a printed format. Therefore, axial velocity fields are presented in this section (with radial velocity components in the vector images) for the central plane only, as the flow unique to breakdown occurs mostly in that plane. The use of three dimensional measurements is still critical, as it ensures data from out-of-plane particle motion is still included.

Figure 4.2 shows velocity profiles on the $r-z$ plane for SV30T1.0 over time. Barring

some small disturbances, presumably due to unsteadiness in the room airflow or surface imperfections in the intake, the flow is relatively steady. In the region where $r/R \leq 0.3$, the axial velocity remains close to the freestream, no-swirl velocity u_∞. Some radial motion can be seen in the first four time steps (shown in the top row of the figure), but that component subsides over time. Outside the core, at $r/R \geq 0.3$, the flow appears in the image to be perfectly axial, as any rotation in the vortex in that plane will only have an out of plane component with no radial velocity. The axial velocity measured is much lower than the freestream velocity, at about $u_z/u_\infty \approx 0.5$. This axial velocity distribution is typical for a vortex, and the lack of breakdown is consistent with the smoke flow visualization results for this case shown in chapter 3, which have shown that any breakdown will occur much further downstream than included in these flow fields. This case provides a useful baseline case for a steady vortex with no breakdown.

Figure 4.3 shows velocity profiles on the $r-z$ plane for SV40T1.0 over time. On initial inspection, the flow is much less steady than the SV30T1.0 case, both in space and over time. In the first four time steps shown in the top row, the area outside the core ($r/R \geq 0.3$) exhibits similar behavior to the steady vortex, with no significant radial component visible and an axial velocity $u_z/u_\infty \approx 0.5$. The core, however appears to contain some small flow recirculation region where the axial velocity is negative, followed by a wake of sorts where the axial flow velocity remains very low, $0 \leq u_z/u_\infty \leq 0.2$. While there is no indication of a specific mode of breakdown, the behavior of the core is consistent with the expected behavior downstream of a breakdown bubble, which may indicate breakdown occurring upstream of the field of view.

The bottom row of flow fields in figure 4.3 shows the evolution of a breakdown bubble. At the upstream portion of the decelerated core, around $z/R = 2.25$, a stagnation point can be seen in the second panel from the left, shown by a white region with the velocity vectors turning to either side of it. As time progresses, that stagnation grows into a region

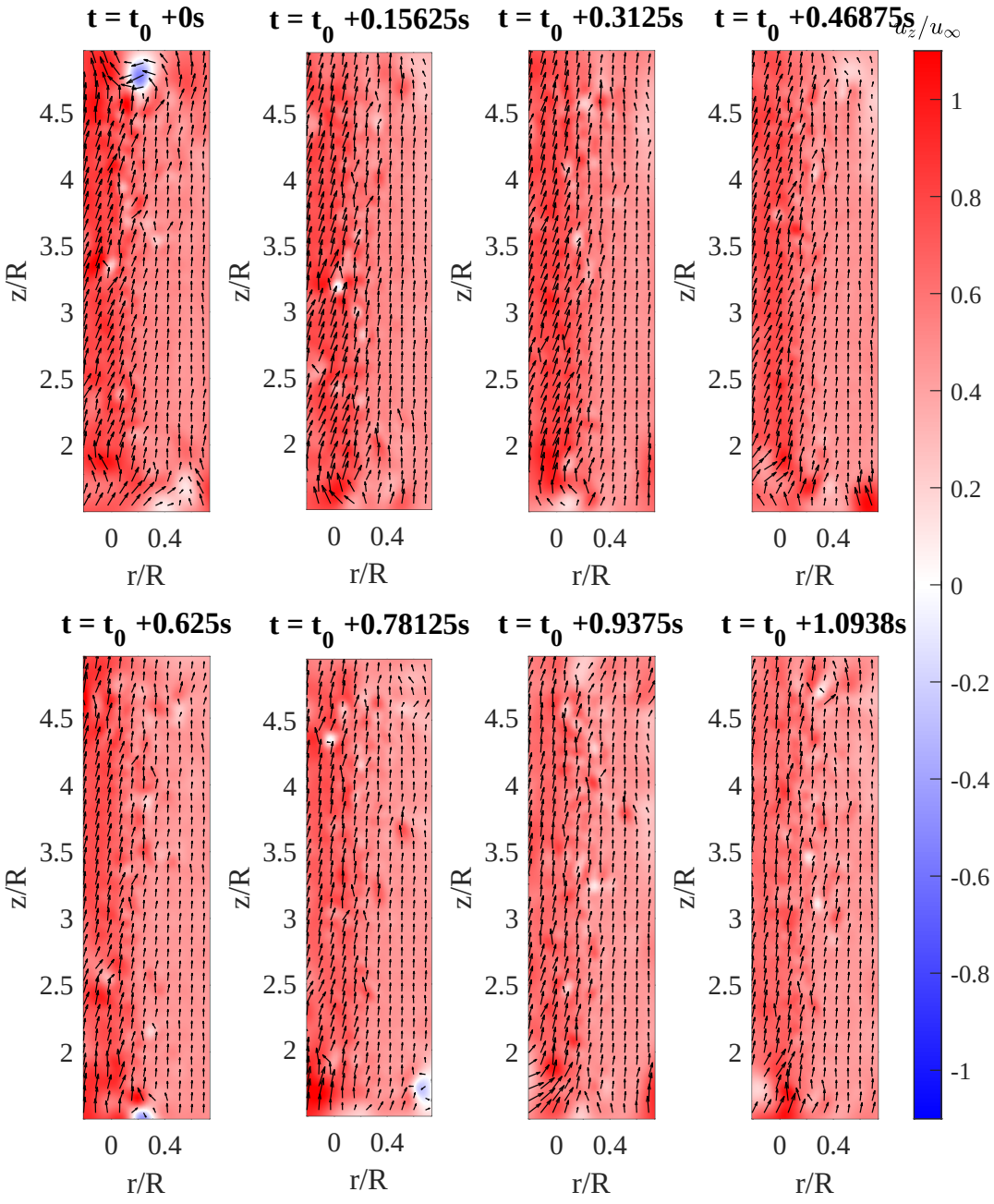


Figure 4.2: Velocity fields in the $r-z$ plane for the SV30T1.0 case over time. The colors represent the axial velocity component u_z and the vectors show the in-plane velocity.

of axially recirculating flow, which grows into a bubble that is slightly wider than the entire original vortex core. Beginning with the second image from the left, as the oncoming axial flow reaches the stagnation point, the flow is diverted around it, forming a shedding pattern reminiscent of flow in the wake of a bluff body. Two counter-rotating vortices, which are part of a 3D vortex ring, can be seen in the final two timesteps. The growth of the bubble causes the flow in the vortex, outside the core, to divert 'around' the region of recirculation, in turn adding a positive radial velocity component, followed by motion in the negative radial direction downstream of the bubble. This behavior is best seen at $t = t_0 + 0.78125s$ and $t = t_0 + 0.9375s$. The radial motion affects the stability of the core, creating secondary instabilities downstream of the bubble. In the final two timesteps, these appear to be a spiral mode. The breakdown structure of a bubble followed by a spiral has been observed many times (e.g. [16]), and is shown in the visualizations in chapter 3.

The process of breakdown and growth of the bubble can be better seen in figure 4.4, which shows the flow fields for SV40T1.0 with higher time resolution, corresponding to the final three timesteps in figure 4.3. The bubble can be seen growing in diameter and axial length, while gradually moving upstream. With the higher time resolution, the vortex pair in the bubble noticeably changes positions, such that the 'tilt' relative to the z axis flips every ≈ 3 timesteps. This behavior of the vortex ring that forms in the bubble is consistent with the unsteady tilting motion observed by Bruecker [3], and appears to happen at a higher frequency than previously estimated, at about $5Hz$ for a full cycle. The growth of the secondary structures in the wake of the bubble is also better seen in this figure, with the radial motion in the vortex appearing first, followed by increased recirculation zones in the core, which grow axially over time.

The flow can be qualitatively visualized in three dimensions with constant velocity contours. A low velocity magnitude region $|U|/u_\infty = 0.2$ roughly corresponds to the outer surface of the stagnation streamlines. Such a contour is shown in figure 4.5 using the

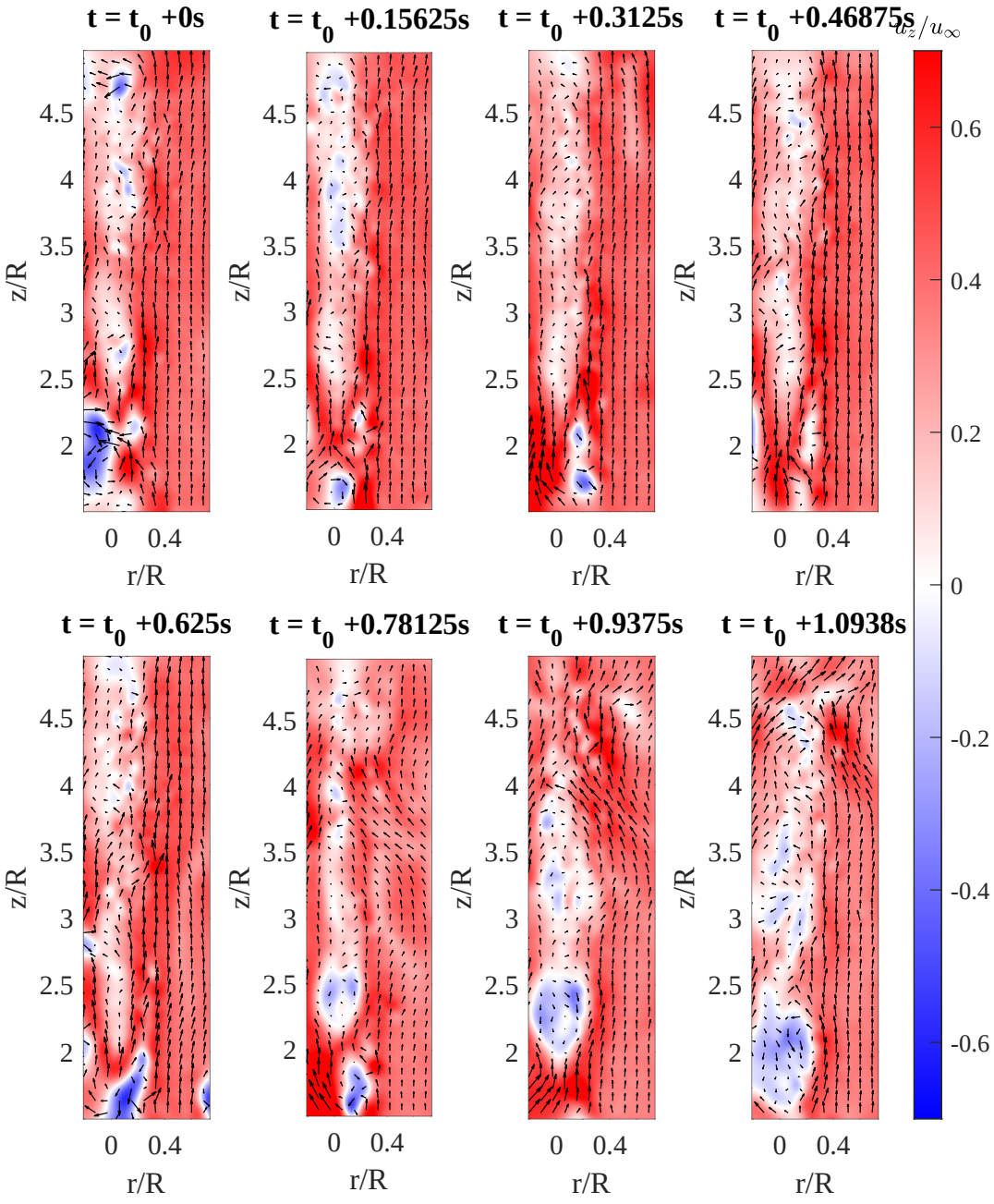


Figure 4.3: Velocity fields in the $r-z$ plane for the SV40T1.0 case over time. The colors represent the axial velocity component u_z and the vectors show the in-plane velocity.

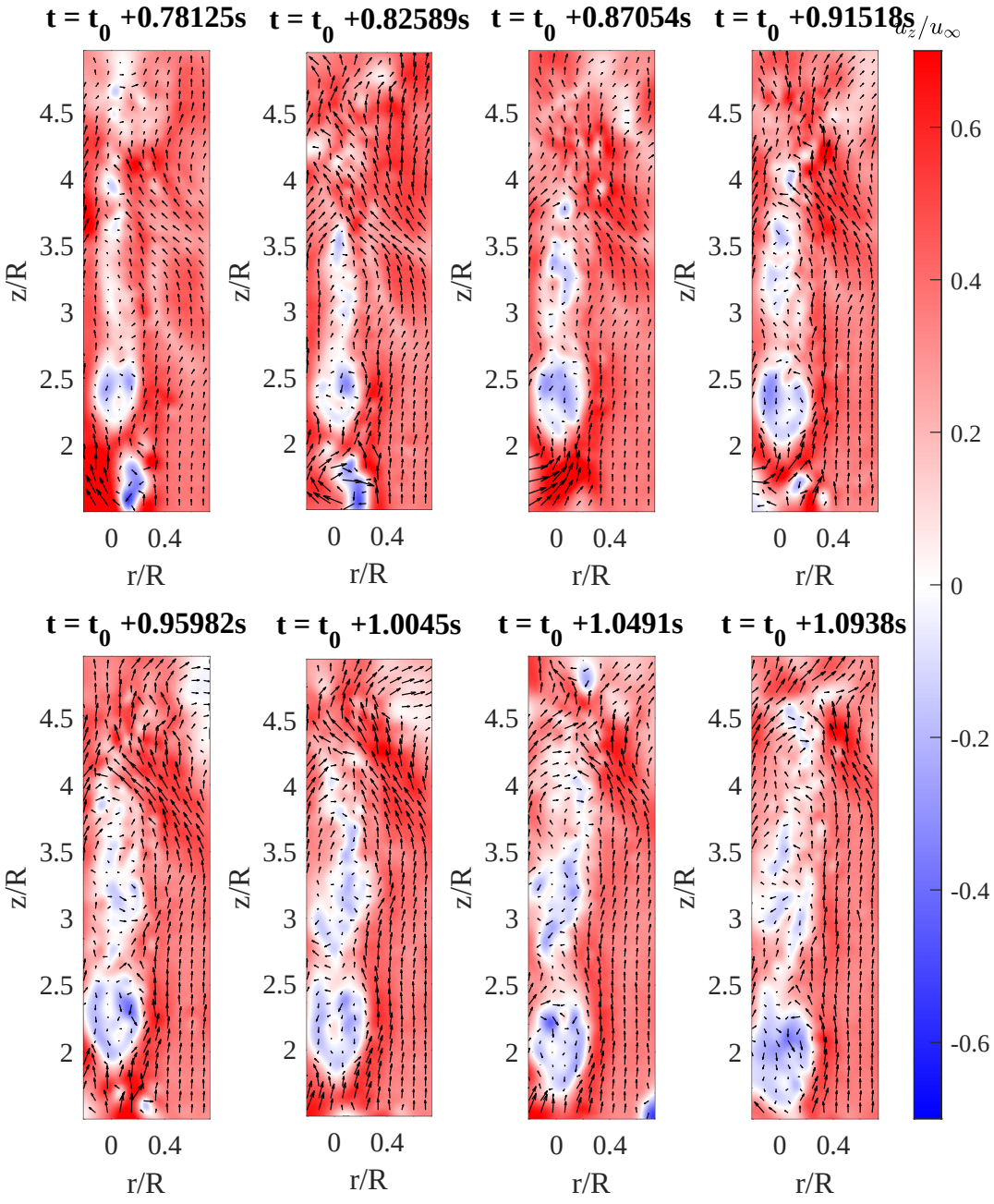


Figure 4.4: Velocity fields in the $r-z$ plane for the SV40T1.0 case with increased time resolution around time of peak breakdown bubble visibility. The colors represent the axial velocity component u_z and the vectors show the in-plane velocity.

SV40T1.0 velocity fields at $t = t_0 + 0.95s$. The overall outer shape of the breakdown bubble can be seen around $2 \leq z/R \leq 2.5$, followed by a smaller stagnant core emanating downstream from the center of the bubble. The core appears mostly axial with minor lateral perturbations, which grow as it expands to a larger unsteady stagnation region. This flow structure appears similar to 2D visualizations and measurements shown in experiments in literature [27] [10] and this thesis.

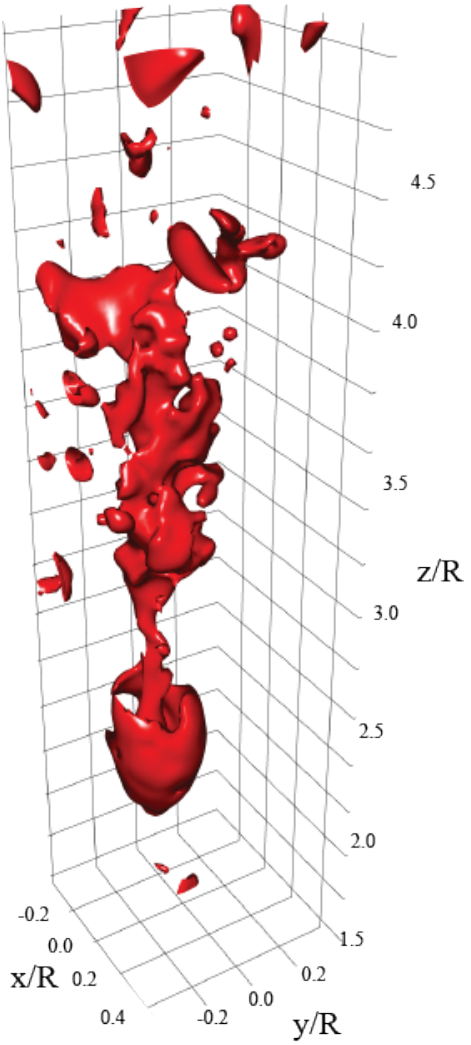


Figure 4.5: 3-D constant velocity contour for the SV40T1.0 case at time $T = t_0 + 0.95s$ indicating the near-stagnation regions in the flow

Figure 4.6 shows velocity profiles on the $r-z$ plane for SV50T1.0 over time. A stag-

nation point and small recirculation zone can be seen in the first time step, slightly growing and moving upstream quickly. A bubble mode breakdown does not appear, but is likely forming upstream of the field of view due to the increased swirl, as seen in the visualizations in chapter 3. The slowed down core is consistent with flow in the wake of a breakdown bubble, yet unlike the lower swirl SV40T1.0 case, the wake appears much more stable with fewer secondary structures. There are two possibilities for this observed behavior. The data set may have captured a specific time range in which the wake was more stable during a periodic cycle. Alternatively, the increased circulation number caused by the increasing swirl vane angle in this case, SV50T1.0, may change the region of breakdown occurrence as proposed by Sarpkaya [27] and shown in chapter 3 from the hysteresis zone to a region of bubble breakdown only.

Figure 4.7 shows velocity profiles on the $r-z$ plane for SV40T1.1 over time, to examine the effects of increased heater temperature on the flow. For this case, the field of view was moved axially downstream in the test section to account for the reduced swirl angle and delayed breakdown. Much like the unheated case, the measured flow appears to be highly unsteady. However, the breakdown bubble seems to move downstream quickly, rather than the slow upstream motion seen in other cases. A small recirculation bubble followed by a spiral mode can be seen in the first timestep. That structure quickly dissipates, and only a small stagnation point remains. The stagnation point then gradually grows into a bubble while moving downstream before dissipating again. In the later timesteps, shown in the bottom row, the upstream section of the core appears to reform with flow similar to the vortex case SV30T1.0. This region slowly grows as the stagnation point moves downstream. At times later than shown in the figure, the flow appears to match the vortex flow in SV30T1.0. Qualitatively, it seems that in addition to the delayed breakdown, the heating increases the frequency of formation of the bubble. This unique instance of a bubble forming and moving upstream quickly provides valuable data, as it allows comparison of

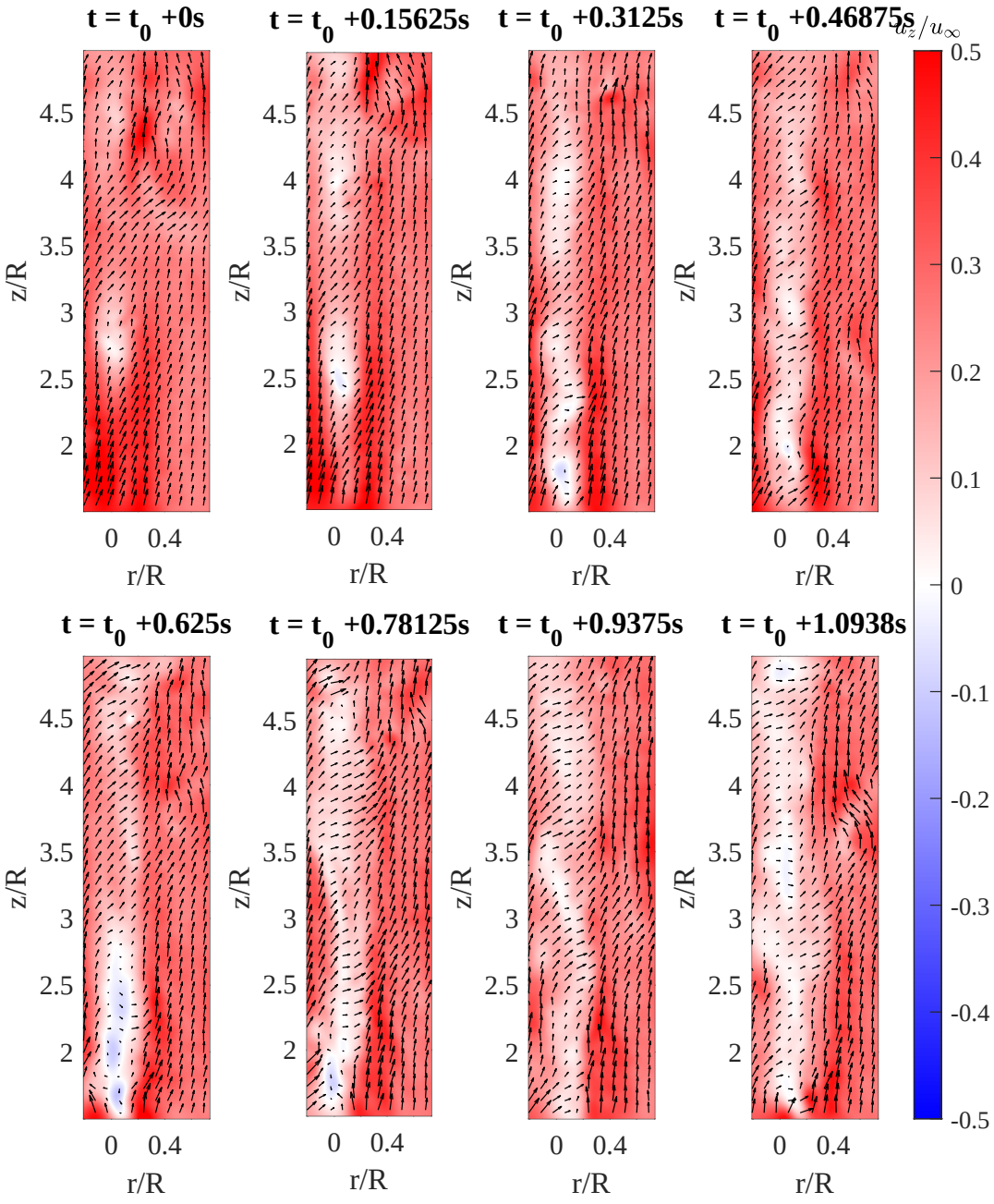


Figure 4.6: Velocity fields in the $r-z$ plane for the SV50T1.0 case over time

flow upstream, downstream, and in the bubble with one relatively short measurement. Such comparisons are presented and discussed in section 4.3.

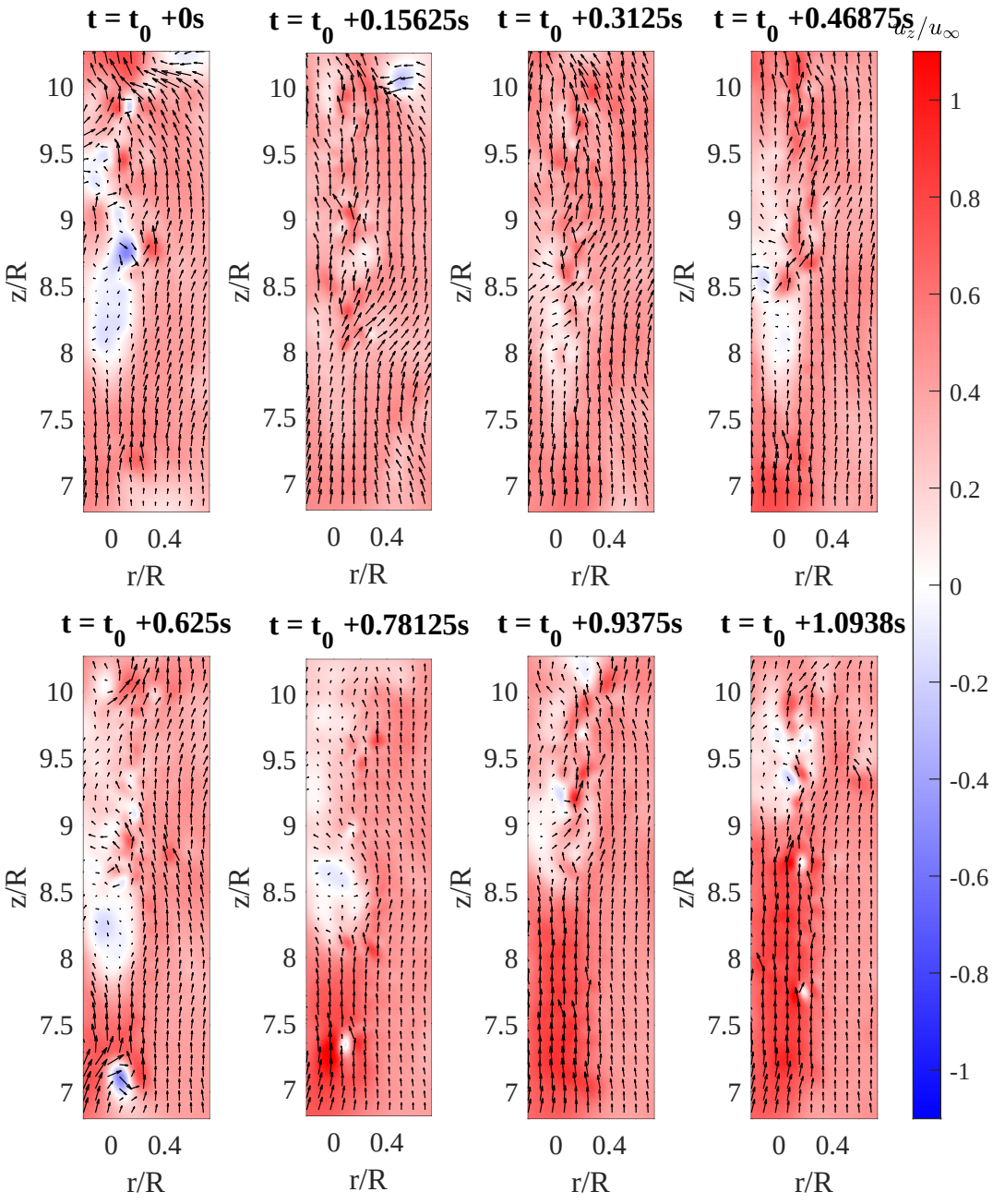


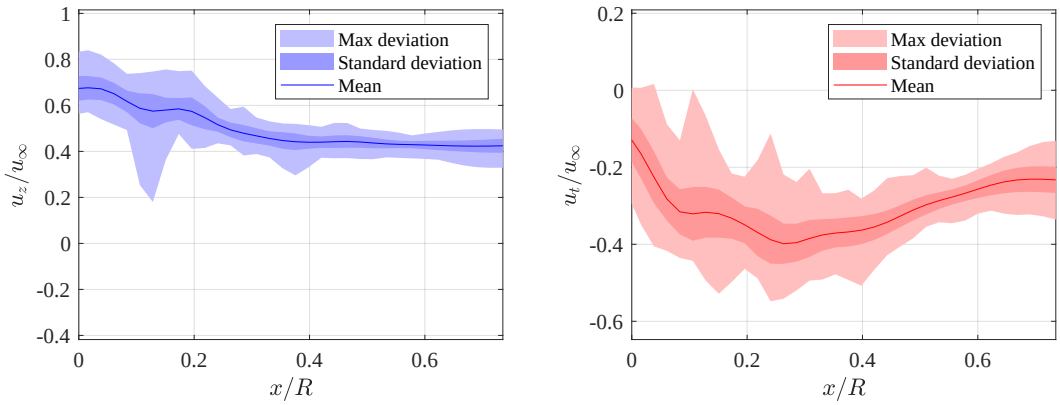
Figure 4.7: Velocity fields in the $r-z$ plane for the SV40T1.1 case over time

4.3 Velocity Profile Analysis

Specific velocity profiles can be extracted from the flow fields and investigated individually to study flow structures, or analyzed over time to determine flow instabilities. In this section, the axial and tangential velocities of a single profile along the test section radius extracted from the SV40T1.1 case is investigated to identify velocity profiles upstream, downstream, and in the breakdown bubble. These profiles are compared to the vortex velocity profiles found for SV30T1.0.

Figure 4.8 shows the time averaged velocity profiles along the radius for the vortex in SV30T1.0. In each plot, the line depicts the mean velocity over the radial positions, the dark shaded area shows the standard deviation for each position, and the light shaded area shows the maximum deviation. Figure 4.8a shows the axial velocity distribution in blue. As expected for a vortex, the core axial velocity remains slightly higher than outside of it. The standard deviation remains $\leq \pm 0.1$ in the core and smaller than that outside of it suggesting relatively steady flow throughout the entire data set. Figure 4.8b shows the tangential velocity distribution in red. Note that the tangential velocity is negative, as the swirl generator induces couter-clockwise swirl. The standard deviation is minimal, and the maximum deviation appears to remain within the overall flow shape. The time-averaged velocity profile is indicative of a vortex model more physical than a classical one such as the Rankine model, though a larger data sample may be required to accurately fit the flow to a specific model.

Figure 4.9 shows the velocity field on the $r-z$ plane for SV40T1.1 at three distinct time steps, such that a single velocity profile at $z/R = 9$ will measure the velocity downstream, at, and upstream of the bubble, respectively (from left to right in the figure). The corresponding velocity profiles are shown in figure 4.10. Figure 4.10a shows the axial velocity profiles. The red line shows the axial velocity upstream of the breakdown. The velocity



(a) Axial velocity, u_z/u_∞ (b) Rotational velocity, u_θ/u_∞

Figure 4.8: Mean velocity profiles along the radius at $z/R = 9$ for the vortex in SV30T1.0

distribution is similar to the time averaged velocity measured in the vortex shown in fig. 4.8a, with a slightly higher peak axial velocity in the core, which could be due to the buoyancy effects of the heating. The blue line shows the axial velocity distribution in the wake of the bubble, resulting in a non-uniform distribution characterized by slow axial velocities overall with an apparent stagnation between the wake and the vortex, which appears mostly unchanged. The axial velocity at the breakdown bubble is shown in magenta. As expected from the velocity fields, a region of flow recirculation is evident by the negative axial velocity at $x/R \leq 0.1$. Outside the bubble, at $x/R \geq 0.45$, the velocity approaches the flow velocity of the vortex. In between, a local peak in axial velocity can be seen, corresponding to the flow that is diverted 'around' the stagnation point and accelerated into the wake. While this plot indicates a loss of total mass flux during breakdown, it is possible that higher velocities exist beyond the radial positions for which velocity was measured, or that the flow is not axisymetric, and mass flux is not evenly distributed along all radii.

Figure 4.10b shows the tangential velocity distributions at the three timesteps in fig. 4.9. Similar to the axial velocity trends, the red line showing the tangential velocity upstream of the breakdown follows the same trend as the mean velocity in the vortex. The magnitude

of the velocity increases up to the edge of the core, estimated from the flow fields around $x/R = 0.2$, then reduces to a somewhat constant value outside the core. The blue line shows the tangential velocity downstream of the bubble. There appears to be a reversal in the direction of rotation in the core, while far outside the core the velocity approaches the pre-breakdown values. The magenta line shows the velocity at the breakdown bubble. As expected, there is no rotation in the axially recirculating portion of the bubble, with rings of counter-rotation around it, before the velocity approaches the vortex values far outside the breakdown occurrence. This indicates that in addition to the effects seen in the $r-z$ plane velocity fields, the breakdown bubble changes the rotation of the flow significantly.

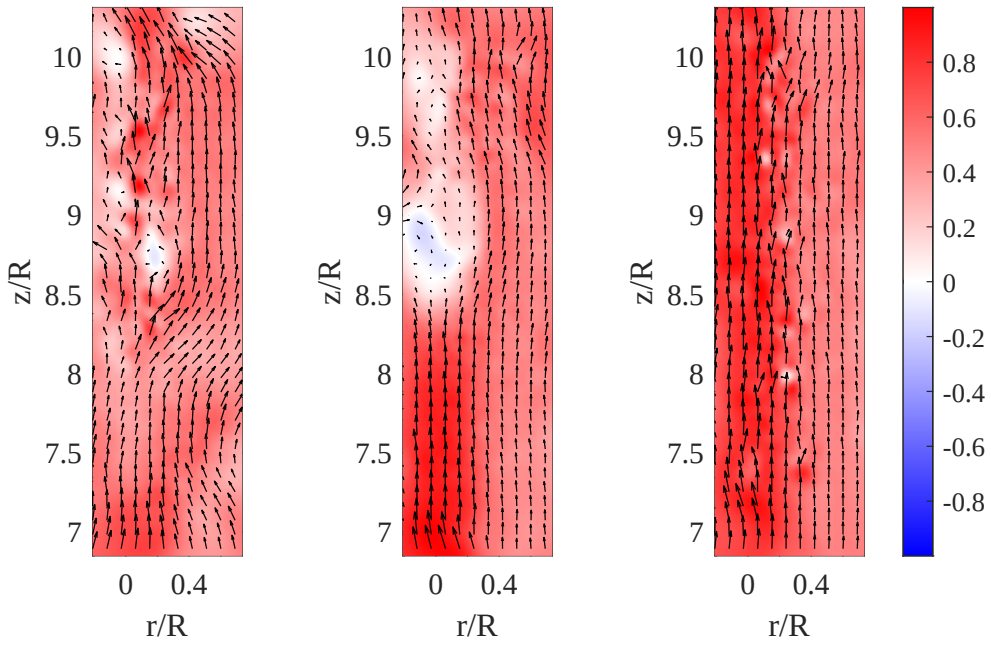
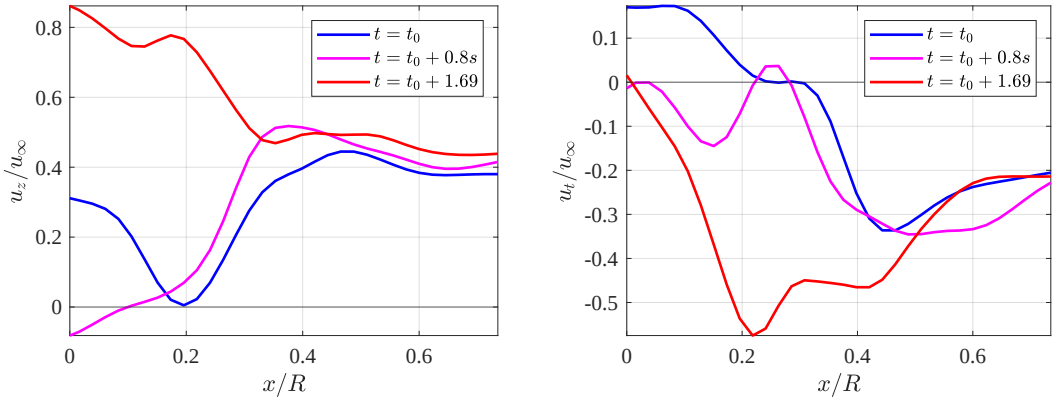


Figure 4.9: Velocity fields in the $r-z$ plane for the SV40T1.1 case before, during and after the breakdown passes through the field of view

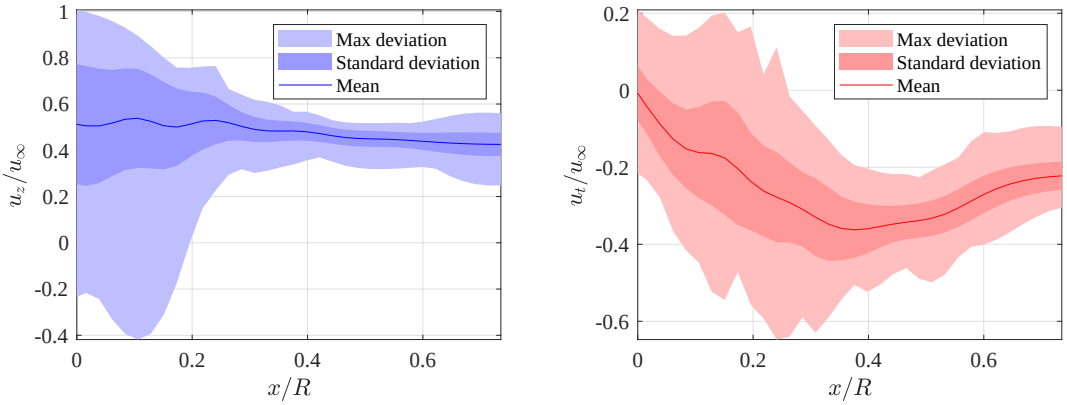
Figure 4.11 shows the time averaged velocities along the radius for SV40T1.1. Since, for the majority of the measurement time, the field of view contained mostly the vortex upstream of the breakdown bubble, the mean profiles are similar in shape to those found for



(a) Axial velocity, u_z/u_∞ (b) Rotational velocity, u_θ/u_∞

Figure 4.10: Select velocity profiles along the radius at $z/R = 9$ for the SV401.1 case corresponding to the flow fields shown in fig. 4.9.

SV30T1.0 shown in fig. 4.8. However, figure 4.11a shows the axial velocity profile, which is influenced by the breakdown bubble's stagnation and reverse flow region, resulting in a lower mean velocity in the core. The significant variations in the axial velocity near the core are also apparent by the increased standard deviation ≈ 0.25 and even greater maximum deviation relative to the vortex case. Similarly, the increased deviations can be seen for the tangential velocity in figure 4.11b. Overall, the breakdown case appears significantly more unsteady than the vortex case.



(a) axial velocity, u_z/u_∞ (b) Rotational velocity, u_θ/u_∞

Figure 4.11: Mean velocity profiles along the radius at $z/R = 9$ for the vortex in SV40T1.1

4.4 Proper Orthogonal Decomposition and Reconstruction

Use of Proper Orthogonal Decomposition (POD) to investigate PTV flow fields may be useful to identify the more 'important' energetically dominant modes of the flow, and reconstruct the main coherent structures of the flow, presumably without losing any time dependency of the data [8]. In this section, POD is used to reconstruct the breakdown bubble contour using the dominant modes in the flow, to compare the experimental results with lower fidelity experimental results and lower noise computational ones.

Figure 4.12 shows the velocity fields in the $r-z$ plane for the first four POD modes identified in SV401.0, where breakdown is observed for the majority of the data set. The corresponding coefficient time histories for each mode are smoothed with a moving average low pass filter and shown in figure 4.13. The first mode may be showing the gradual upstream motion of the entire flow structure observed in the raw flow fields. It contains a strong upstream velocity and its coefficient is highest at the time of the largest breakdown bubble occurrence. The second mode seems to correspond to the vortex flow with a recirculation bubble, which may be the large scale breakdown structures. It is difficult and

ill-advised to assign physical meaning to higher POD modes where it is not immediately clear, but modes 3 and 4 appear to contain some aspect of the stagnation point and flow around it, as well as some flow structures downstream of the bubble. From the coefficient time history plot in fig. 4.13, it can be seen that higher order modes have a higher frequency. In order to compare the reconstructed data to Bruecker's findings, which were limited to a sampling frequency of $10Hz$ (which should capture flow behaviour up to $5Hz$, following the Nyquist criterion), no higher order modes were used, as their time histories had higher frequency components.

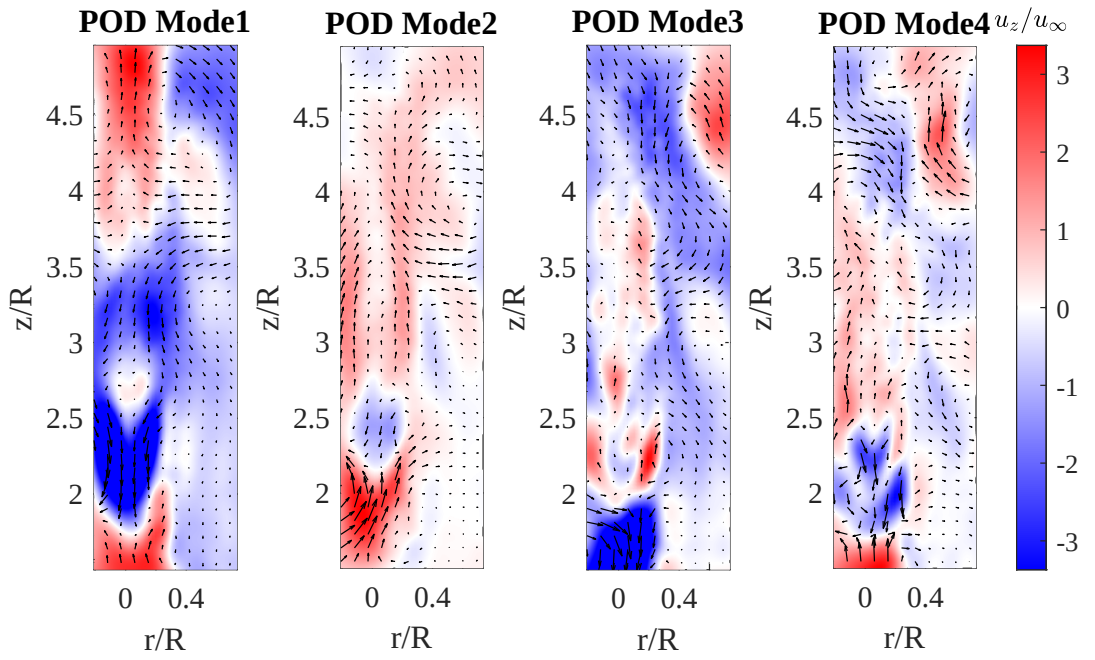


Figure 4.12: Velocity fields in the $r-z$ plane for the first four POD modes

Figure 4.14 shows the constant velocity ($|U|/u_\infty = 0.2$) contour for SV40T1.0 at $t = t_0 + 0.95s$ reconstructed using the first four POD modes. Compared to the original contour shown in fig. 4.5, the bubble appears to be smooth and almost perfectly axissymetric. Rather than a spiraling, unsteady wake, the wake appears to be somewhat axisymetric and expands smoothly downstream. The reconstructed contour is similar in shape to most low

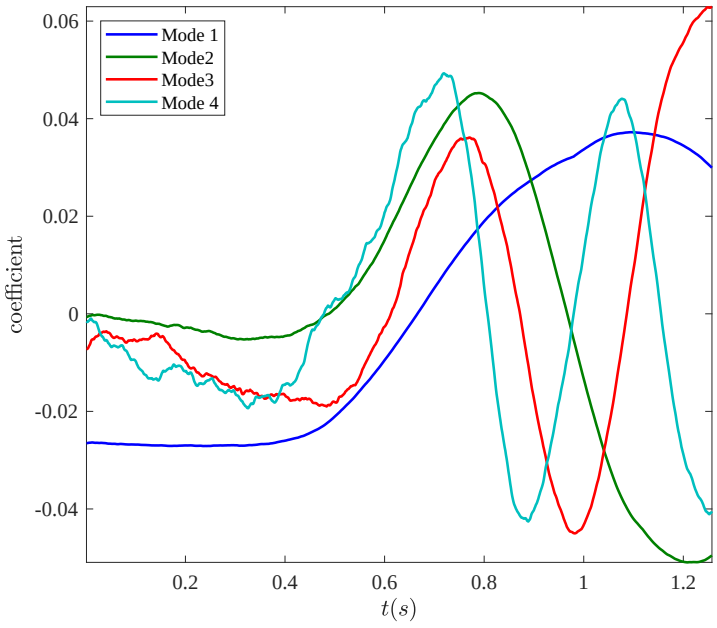


Figure 4.13: Time coefficients for the first four POD modes, smoothed with a moving average low pass filter.

time resolution visualizations ([10] [16] [3]). One such visualization is presented in figure 4.15, which shows an image of a bubble captured by Sarpkaya [27] at $10\,Hz$ and a similar Reynolds number range to the experiments in this thesis. While it is possible that the additional details in the original measurements are due to noise that is removed through the POD process, it is likely that higher order modes - corresponding to higher frequency phenomenons - which were previously not included in measurements and may be ignored in computational models, have a critical effect on the breakdown process and resulting flow strucure.

4.5 Chapter Summary

This chapter presented flow fields extracted from PTV measurements for cases with and without observed breakdown, which were intended to investigate the flow structures

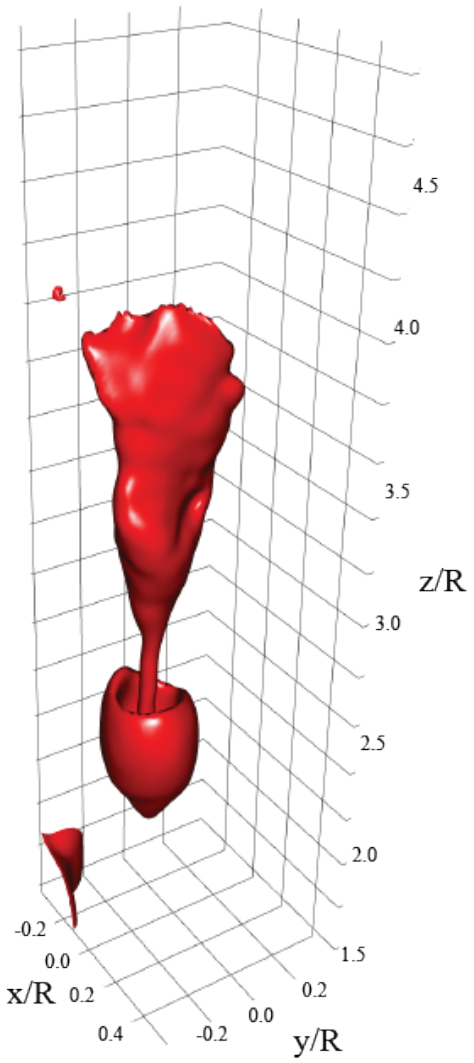


Figure 4.14: 3-D constant velocity contour for the SV40T1.0 case at time $T = t_0 + 0.95s$ using the reconstructed flow fields from the first four POD modes

in the breakdown process and evaluate the significance of the high time resolution this experimental technique provides. Individual velocity profile were investigated over time to assess the changes and unsteadiness of the flow during breakdown. POD was used to filter out modes that contain high frequency motion, to compare the results found in this study to previous results with lower time resolution.

The flow fields presented shown a detailed time-lapse of the breakdown bubble growth,



Figure 4.15: Image of a breakdown bubble at $Re_t = 6500$ captured at $10\,Hz$, from [27]

as well as the effects of the vortex flow around the bubble on the secondary flow structures downstream of it. The observed structures are consistent with those identified in previous experimental work. The breakdown bubble was shown to be mostly axissymetric, but with a slight periodic tilting of the vortex ring that forms it. **The bubble was shown to move upstream with a higher swirl vane angle, and downstream with flow heating, in a similar manner to the behavior identified in chapter 3.**

The velocity profiles analyzed for SV40T1.1 were used to compare the flow upstream, downstream, and in the breakdown bubble. Upstream of the breakdown, the flow was similar to the no-breakdown vortex flow. At the bubble, axial flow recirculation was measured, with the tangential velocity stagnating. Downstream of the bubble, the axial flow recovers slightly but remains slower than the vortex core axial velocity. A comparison of the time averaged velocity profiles between SV40T1.1 and SV30T1.0 showed significantly higher

standard deviation and maximum deviation for the breakdown case of SV40T1.1, indicating very unstable behaviour throughout the breakdown process.

The flow fields were reconstructed using the first four POD modes, which correspond to lower frequency flow behaviors that would have been captured in previous experiments. The reconstructed flow structure is very similar to previously measured cases of breakdown.

The results shown in this chapter indicate that the higher time resolution, available due to the design of the new vortex rig and use of PTV with Shake-The-Box, provides new information on the breakdown process than may have previously been unattainable with lower time resolution techniques.

Chapter 5: Conclusions

This thesis focused on experimental investigations of the effects of heat addition on vortex breakdown, and the use of high-speed time resolved measurements to characterize the breakdown behavior. To the extent of the author's knowledge, this study is the first example of three-dimensional time-resolved measurements of vortex breakdown, establishing the importance of high time resolution data in the effort to fully understand breakdown onset and mechanisms. The study also investigates non-isothermal vortex breakdown behavior to offer a glimpse into whether breakdown, and potentially the blue whirl, can be controlled with heat addition. The following sections include a summary of the presented work, along with suggestions for future work.

5.1 Summary

To carry out the goals of this thesis, a novel experimental rig was designed and tested. The vortex breakdown rig and its design process were presented in chapter 2. The rig design was based on a proven rig primarily used for flow visualizations. First, the design was adapted for multi-camera velocimetry experiments, which required a redesign of the drive section for laser illumination optical access and a smooth test section surface with no instrument access ports. The intake was redesigned to include a non-intrusive inflow constant temperature heater. Instabilities induced by fan vibrations led to a redesign of the drive section, resulting in a compact and straightforward to construct fan unit that simpli-

fied the process of adjusting the PTV field of view. The final rig, in addition to fulfilling the demanding requirements set by the desired experiments, makes vortex breakdown experiments more accessible, as it is primarily made of 3D printed parts and off the shelf components, and thus can be easily duplicated for broader use.

Smoke flow visualization images were presented in chapter 3. These visualizations were used to qualitatively identify the effects of changing the intake swirl vane angle or the heater temperature on breakdown occurrence and behavior. Increasing the swirl vane angle was shown to cause breakdown and move the initial breakdown point upstream while making the breakdown bubble larger. Increasing the heater temperature had the opposite effect, suppressing the breakdown partially or outright. The images were used to estimate the flow swirl angle, and a summary of the measured angles was shown. At higher swirl vane angles, the rate of swirl reduction with heat was increased. The decrease in flow swirl angle with increasing temperature is explained using the Boussinesq assumption simplified Navier-Stokes equation, which shows that the buoyancy effects of the heating induce a favorable pressure gradient, increasing the axial velocity and in turn reducing the flow swirl angle. This chapter identified cases of interest for further investigation and proposed a framework to approach heating experiments.

Three-dimensional time-resolved flow fields from Particle Tracking Velocimetry measurements were presented in chapter 4. The use of PTV with the Shake-The-Box algorithm for processing allowed higher acquisition rates than any prior study. Flow fields of the breakdown process for select cases were shown, and differences in the breakdown process with different swirl settings or heating values were discussed. The breakdown bubble was shown to exhibit similar behavior and topology to previously proposed models, but with higher oscillation frequencies. Velocity profiles upstream, downstream, and in the breakdown bubble were studied and compared to the velocity in a coherent vortex, showing significant unsteadiness in the flow. Proper Orthogonal Decomposition was used to

identify the lower frequency modes in the flow. When reconstructed using those modes only, the flow appeared similar to structures observed in prior works that were limited to those lower frequencies. The time-resolved measurements presented show the importance of high time resolution measurements to fully explain the vortex breakdown phenomenon. In a field where there is limited understanding into the cause and process of the breakdown, the adaptation of well established experiments for use of modern tools that enhance the scope of data that can be collected is crucial for expanding the body of knowledge and answer new research questions.

5.2 Open Problems and Suggestions for Future Work

The work presented in this thesis unlocks a whole range of new aspects of vortex breakdown that can be studied. This section proposes some future avenues of research.

1. Due to the complexity of the flow, any experiment relies on a large number of independent variables. In the present study, only swirl vane angle and heater temperature were varied, but many more variables can be tested to determine their effect on the flow in order to generalize the results as much as possible. While some parameters may be more easily investigated with computational methods, such as test section diameter and its influence on wall effects, others are more suitable for experimental measurements, such as Reynolds number changes or intake flow conditioning effects.

2. This study led to the assumption that heating effects can be approximated purely as creating a favorable pressure gradient causing an increase in axial velocity. To verify this theory, cases can be compared where a similar flow Reynolds number is reached either by using heating or by increasing the fan speed, to identify any possible heating effects other than the increased axial velocity.

3. The buoyancy effects on the flow caused by the heating can also be investigated by simply flipping the entire rig such that the test section flows with gravity. While such an experiment will require some redesigning of the rig, it may provide straightforward results.

4. The simulations which motivated this work applied heating directly to the breakdown bubble, rather than upstream of it as was done in this work. Therefore, if a method to heat the bubble directly, while adding significantly more heat to it, can be developed, similar effects to those found in the simulations may be achieved.

5. A considerable amount of experimental data was collected for this work, and not used due to the high processing times required for STB. That raw data, and the data used in this thesis can also be further analyzed to study the vortex breakdown process. For example - a vortex detection criterion can be applied to the flow fields to identify the vortex ring in the bubble and track it over time, producing precise, time-resolved information regarding the bubble growth and motion for each case. The data can also be used to identify flow swirl angles to verify the trends found from smoke flow visualizations.

Appendix A: Heater Characterization

This Appendix presents temperature and velocity characterization data for the SV00T13 case, to explain the assumption stated in chapter 2 that the heat and the velocity induced by it are uniform. Temperature measurements and PTV velocity measurements were collected with the swirl vane angle $\theta_{SV} = 0$. Figure A.1 shows the resulting velocity field, time averaged over a half second. The flow velocity appears uniform, and indeed remains uniform throughout the measured volume. Figure A.2 shows the measured ratio of local temperature over freestream temperature T/T_∞ in the $r-z$ plane. The measurements appear uniform, apart from a minimal increase when the sensor is closest to the heater, around $x/R = Z/R = 0$, however, it still remains within the approximated sensor error.

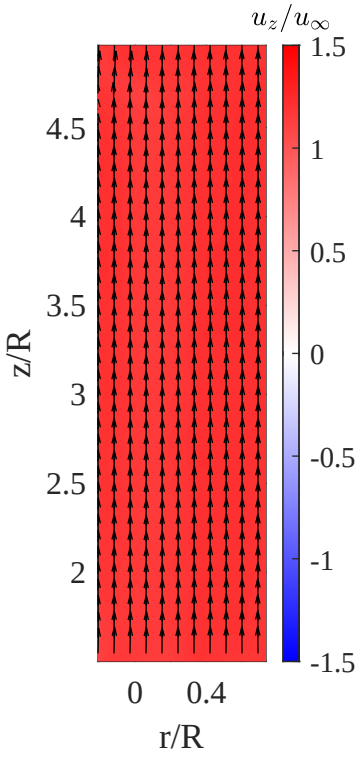


Figure A.1: Time-Averaged velocity field for case SV00T13, The colors represent the axial velocity component u_z and the vectors show the in-plane velocity

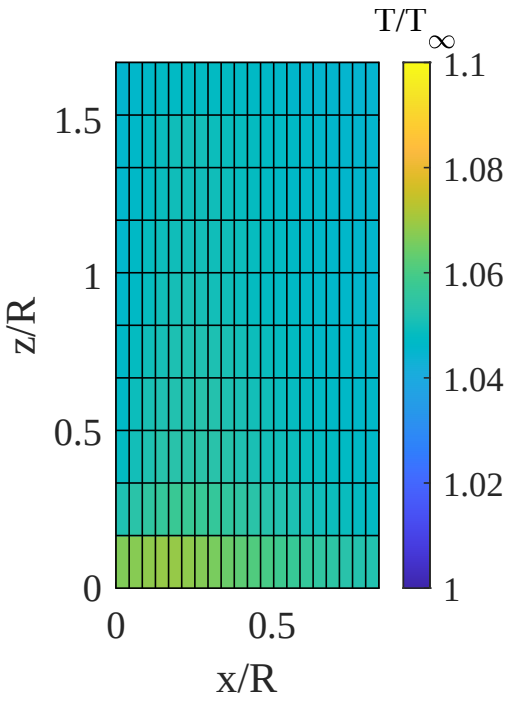


Figure A.2: Temperature map at the $r-z$ plane measured with $T_h = 323K$

Bibliography

[1] Francine Battaglia, Kevin B McGrattan, Ronald G Rehm, and Howard R Baum. Simulating fire whirls. *Combustion Theory and Modelling*, 4(2):123, 2000.

[2] Francine Battaglia, Ronald G. Rehm, and Howard R. Baum. The fluid mechanics of fire whirls: An inviscid model. *Physics of Fluids*, 12(11):2859–2867, 2000.

[3] Ch Brücker and W Althaus. Study of vortex breakdown by particle tracking velocimetry (PTV). *Experiments in fluids*, 13(5):339–349, 1992.

[4] John J Cassidy and Henry T Falvey. Observations of unsteady flow arising after vortex breakdown. *journal of Fluid Mechanics*, 41(4):727–736, 1970.

[5] Keng Hoo Chuah, Kazunori Kuwana, Kozo Saito, and Forman A. Williams. Inclined fire whirls. *Proceedings of the Combustion Institute*, 33(2):2417–2424, 2011.

[6] Joseph D Chung, Xiao Zhang, Carolyn R Kaplan, and Elaine S Oran. The structure of the blue whirl revealed. *Science Advances*, 6(33):eaba0827, 2020.

[7] Wilfried Coenen, Erik J Kolb, Antonio L Sánchez, and Forman A Williams. Observed dependence of characteristics of liquid-pool fires on swirl magnitude. *Combustion and Flame*, 205:1–6, 2019.

[8] L Cordier and Michel Bergmann. Proper orthogonal decomposition: an overview. *Lecture series 2002-04, 2003-03 and 2008-01 on post-processing of experimental and numerical data, Von Karman Institute for Fluid Dynamics, 2008.*, pages 46–pages, 2008.

[9] Howard W Emmons and Shuh-Jing Ying. The fire whirl. In *Symposium (international) on Combustion*, volume 11, pages 475–488. Elsevier, 1967.

[10] Marcel Escudier. Vortex breakdown: observations and explanations. *Progress in Aerospace Sciences*, 25(2):189–229, 1988.

[11] MP Escudier. Vortex breakdown and the criterion for its occurrence. *Intense Atmospheric Vortices*, page 247, 1982.

[12] James Henry Faler and Sidney Leibovich. An experimental map of the internal structure of a vortex breakdown. *Journal of Fluid Mechanics*, 86(2):313–335, 1978.

[13] MG Hall. Vortex breakdown. *Annual review of fluid mechanics*, 4(1):195–218, 1972.

[14] S. B. Hariharan, P. Anderson, Huahua Xiao, Michael J. Gollner, and Elaine S. Oran. The blue whirl: Boundary layer effects, temperature and oh* measurements. *Combustion and Flame*, 203:352–361, April 2019.

[15] Sriram Bharath Hariharan, Evan T Sluder, Michael J Gollner, and Elaine S Oran. Thermal structure of the blue whirl. *Proceedings of the Combustion Institute*, 37(3):4285–4293, 2019.

[16] JK Harvey. Some observations of the vortex breakdown phenomenon. *Journal of Fluid Mechanics*, 14(4):585–592, 1962.

[17] Miguel Angel Herrada and Vladimir Shtern. Control of vortex breakdown by temperature gradients. *Physics of Fluids*, 15(11):3468–3477, 2003.

[18] Yu Hu, S. B. Hariharan, Haiying Qi, Michael J. Gollner, and Elaine S. Oran. Conditions for formation of the blue whirl. *Combustion and Flame*, 205:147–153, June 2019.

[19] Ying Huang and Vigor Yang. Dynamics and stability of lean-premixed swirl-stabilized combustion. *Progress in energy and combustion science*, 35(4):293–364, 2009.

[20] E Krause. A contribution to the problem of vortex breakdown. *Computers & fluids*, 13(3):375–381, 1985.

[21] Assaf Krupnik and Anya R Jones. Time-resolved particle image velocimetry measurements of vortex breakdown. In *AIAA SCITECH 2023 Forum*, page 2483, 2023.

[22] Kazunori Kuwana, Satoshi Morishita, Ritsu Dobashi, Keng H Chuah, and Kozo Saito. The burning rate's effect on the flame length of weak fire whirls. *Proceedings of the Combustion Institute*, 33(2):2425–2432, 2011.

[23] Jiao Lei, Naian Liu, Yan Jiao, and Shaojie Zhang. Experimental investigation on flame patterns of buoyant diffusion flame in a large range of imposed circulations. *Proceedings of the Combustion Institute*, 36(2):3149–3156, 2017.

[24] MV Lowson. Some experiments with vortex breakdown. *The Aeronautical Journal*, 68(641):343–346, 1964.

[25] O Lucca-Negro and T O'doherty. Vortex breakdown: a review. *Progress in energy and combustion science*, 27(4):431–481, 2001.

[26] Lothar Rukes, Moritz Sieber, C Oliver Paschereit, and Kilian Oberleithner. The impact of heating the breakdown bubble on the global mode of a swirling jet: Experiments and linear stability analysis. *Physics of Fluids*, 28(10):104102, 2016.

[27] Turgut Sarpkaya. Vortex breakdown in swirling conical flows. *AIAA journal*, 9(9):1792–1799, 1971.

[28] Daniel Schanz, Sebastian Gesemann, Andreas Schröder, Bernhard Wieneke, and Matteo Novara. Non-uniform optical transfer functions in particle imaging: calibration and application to tomographic reconstruction. *Measurement Science and Technology*, 24(2):024009, 2012.

[29] Daniel Schanz, Andreas Schröder, Sebastian Gesemann, Dirk Michaelis, and Bernhard Wieneke. Shake the box: a highly efficient and accurate tomographic particle tracking velocimetry (tomo-ptv) method using prediction of particle positions. 2013.

[30] A Yu Snegirev, JA Marsden, J Francis, and GM Makhviladze. Numerical studies and experimental observations of whirling flames. *International journal of heat and mass transfer*, 47(12-13):2523–2539, 2004.

[31] S Soma and K Saito. Reconstruction of fire whirls using scale models. *Combustion and Flame*, 86(3):269–284, 1991.

[32] L Talbot. Laminar swirling pipe flow. *Journal of Applied Mechanics*, 1954.

[33] IM Titchener and AJ Taylor-Russell. Experiments on the growth of vortices in turbulent flow. *ARC Technichal Report*, 1957.

[34] David J Tritton. *Physical fluid dynamics*. Springer Science & Business Media, 2012.

[35] Huahua Xiao, Michael J Gollner, and Elaine S Oran. From fire whirls to blue whirls and combustion with reduced pollution. *Proceedings of the National Academy of Sciences*, 113(34):9457–9462, 2016.

[36] Xiao Zhang, Joseph D Chung, Carolyn R Kaplan, and Elaine S Oran. Simulations of vortex breakdown undergoing heat addition and extraction. In *AIAA Scitech 2021 Forum*, 2021.